

# Adaptive Riemannian Optimization for Multi-Scale Diffeomorphic Matching

Rohit Jena<sup>a,d</sup>, Pratik Chaudhari<sup>a,b,\*</sup>, and James C. Gee<sup>a,c,d,\*</sup>

<sup>a</sup>Computer and Information Science, University of Pennsylvania

<sup>b</sup>Electrical and Systems Engineering, University of Pennsylvania

<sup>c</sup>Radiology, Perelman School of Medicine, University of Pennsylvania

<sup>d</sup>Penn Image Computing and Science Laboratory, University of Pennsylvania

\*Corresponding Authors: [pratikac@upenn.edu](mailto:pratikac@upenn.edu), [gee@upenn.edu](mailto:gee@upenn.edu)

May 6, 2025

## Abstract

The paper proposes FireANTs, the first multi-scale Adaptive Riemannian Optimization algorithm for dense diffeomorphic image matching. One of the most critical and understudied aspects of diffeomorphic image matching algorithms are its highly ill-conditioned nature. We quantitatively capture the extent of ill-conditioning in a typical MRI matching task, motivating the need for an adaptive optimization algorithm for diffeomorphic matching. To this end, FireANTs generalizes the concept of momentum and adaptive estimates of the Hessian to mitigate this ill-conditioning in the non-Euclidean space of diffeomorphisms. Unlike common non-Euclidean manifolds, we also formalize considerations for multi-scale optimization of diffeomorphisms. Our rigorous mathematical results and operational contributions lead to a state-of-the-art dense matching algorithm that can be applied to generic image data with remarkable accuracy and robustness. We demonstrate consistent improvements in image matching performance across a spectrum of community-standard medical and biological correspondence matching challenges spanning a wide variety of image modalities, anatomies, resolutions, acquisition protocols, and preprocessing pipelines. This improvement is supplemented by  $300\times$  to  $3200\times$  speedup over existing CPU-based state-of-the-art algorithms. For the first time, we perform diffeomorphic matching of sub-micron mouse isocortex volumes at native resolution, and generate a  $25\mu m$  mouse brain atlas in under 25 minutes. Our fast implementation also enables hyperparameter studies that were intractable with existing correspondence matching algorithms.

**Keywords:** correspondence matching, deformable image matching, diffeomorphisms, optimization, non-Euclidean manifold, microscopy, neuroimaging

## 1 Introduction

The ability to identify and map corresponding elements across diverse datasets or perceptual inputs – known as *correspondence matching* – is fundamental to interpreting and interacting with the

world. Correspondence matching between images is one of the longstanding fundamental problem in computer vision. Influential computer vision researcher Takeo Kanade famously once said that the three fundamental problems of computer vision are: “Correspondence, correspondence, correspondence”<sup>1</sup>. Indeed, correspondence matching is fundamental and ubiquitous across various disciplines, manifesting in many forms including but not limited to stereo matching<sup>2</sup>, structure from motion<sup>3,4</sup>, template matching<sup>5</sup>, motion tracking<sup>6,7</sup>, shape correspondence<sup>8</sup>, semantic correspondence<sup>9</sup>, point cloud matching<sup>10</sup>, optical flow<sup>11</sup>, and deformable image matching<sup>12</sup>. Solving these problems addresses the desiderata for a wide range of applications in computer vision, robotics, medical imaging, remote sensing, photogrammetry, geological and ecological sciences, cognitive sciences, human-computer interaction, self-driving among many other fields.

Correspondence matching is broadly divided into two categories: sparse and dense matching. Most sparse matching problems like stereo matching, structure from motion, and template matching involve finding a *sparse set of salient features* across images followed by matching them. In such cases, the transformation between images, surfaces, or point clouds is typically also parameterized with a small number of parameters, e.g., an affine transform, homography or a fundamental matrix. These methods are often robust to noise, occlusions, and salient features can be detected and matched efficiently via analytical closed forms. In contrast, dense matching is much harder because the entire image is considered for matching and cannot be reduced to a sparse set of salient features, and the transformation between images is typically parameterized with a large number of parameters, e.g., a dense deformation field. Moreover, dense matching is sensitive to local noise, and cannot be solved efficiently via analytical closed forms – necessitating iterative optimization methods<sup>13–18</sup>. Due to the dense and high-dimensional nature, these methods are often plagued with ill-posedness, curse of dimensionality, difficulty in optimization and scalability to high-resolution data.

In this work, we focus on dense deformable correspondence matching, which is the non-linear and local (hence deformable) alignment of two or more images into a common coordinate system. Dense deformable correspondence matching is a fundamental problem in computer vision<sup>19</sup>, medical imaging<sup>20–22</sup>, microscopy<sup>23,24</sup>, and remote sensing. Here, we focus on applications in biomedical and biological imaging. In the biomedical and biological sciences, deformable correspondence matching is also referred to as deformable registration. Within dense deformations, *diffeomorphisms* are of special interest as a family of deformations that are invertible transformations such that both the transform and its inverse are differentiable. This allows us to accurately model the deformation between images and also ensures that the deformation is physically plausible.

We address and tackle two fundamental problems in dense correspondence matching: ill-conditioning and scalability. The ill-conditioning arises due to the high-dimensional and heterogeneous nature of the dense matching optimization objective, that can be mitigated by adaptive optimization methods. Although standard adaptive optimization methods<sup>25,26</sup> are shown to work in fixed Euclidean spaces, it is not obvious how to extend this formulation to the non-Euclidean space of diffeomorphisms. Fortunately, diffeomorphisms admit many interesting mathematical properties like being embedded in a Riemannian manifold, having a Lie Group structure, and local geodesic formulations that can be exploited for adaptive optimization. We present a *novel* and *mathematically rigorous* framework for adaptive optimization of diffeomorphic matching §4.4. This is done by exploiting the group structure of diffeomorphisms to define a custom gradient descent algorithm, followed by adaptive optimization on this space. Second, we observe that most existing state-of-the-art methods are prohibitively slow for high-resolution data, which limits their applicability to rigorous hyperparameter

studies, large-scale data, or high-resolution alignment at mesoscopic or microscopic resolutions. Our novel operational contributions lead to an algorithm that is orders of magnitude quicker than existing state-of-the-art toolkits (Fig. 4) and can perform diffeomorphic matching on high resolution modalities like sub-micron expansion microscopy images (Fig. 3) in minutes, and generate  $25\mu m$  mouse brain volumes atlas in under 25 minutes (§2.4). This quantum leap in speedup and scalability also makes large-scale hyperparameter studies computationally feasible (Figs. 4 and 5). We package our contributions into a software toolkit called **FireANTs**, which is an open-source state-of-the-art toolkit for dense deformable correspondence matching. Our framework can allow a practitioner to perform interactive dense matching that is useful for aligning complex, multimodal, multi-channel or high-resolution images<sup>27,28</sup> or to provide guidance to compensate for missing data (e.g., in microscopy imaging), wherein a typical dense image matching algorithm would fail to run interactively.

## 2 Results

FireANTs represents the next generation of algorithms superseding the widely established and successful adoption of the ANTs ecosystem spanning the gamut of biomedical and life sciences research. Accordingly, we rigorously evaluate FireANTs against established benchmarks to substantiate its efficacy and its viability as a robust registration algorithm across anatomies and modalities. Furthermore, we extend our analysis to encompass datasets with considerably higher image heterogeneity, namely deformable registration of a high-resolution mouse brain isocortex *at submicron resolution*, and generating a  $25\mu m$ -resolution fMOST atlas of the mouse brain in under 25 minutes. Finally, we demonstrate its unprecedented speedup and usability by showing speedups of up to three orders of magnitude and robustness to hyperparameters, subsequently opening avenues in the ability to perform large-scale hyperparameter studies and registration of exceedingly complex and larger datasets.

### 2.1 Experiment Setup

We briefly describe the significance, existing state-of-the-art and challenges associated with the chosen benchmarks to demonstrate the efficacy of FireANTs.

**In-vivo brain mapping challenges**<sup>29,30</sup> Within the biomedical sciences, registration algorithms like ANTs have been predominantly used by the neuroimaging community by far. Klein *et al.*<sup>29</sup> in their landmark paper reported an extensive evaluation of fourteen state-of-the-art registration algorithms on four neuroimaging datasets. The four neuroimaging datasets (IBSR18, CUMC12, MGH10, LPBA40) comprise different whole-brain labelling protocols, eight different evaluation measures and three independent analysis methods. More details about the datasets are outlined in [Appendix A.1](#). ANTs was one of the top performing methods for this challenge, performing well robustly across all four datasets. The Learn2Reg<sup>31</sup> version of the OASIS dataset<sup>30</sup> is another large scale dataset with 414 subjects for inter-subject brain MRI registration. OASIS is routinely used as a training dataset for deep learning algorithms like VoxelMorph<sup>32</sup>. Evaluating on these challenges is therefore imperative to establish FireANTs as an effective, versatile and robust algorithm for neuroimaging applications. In total, we compare with state-of-the-art baselines on over *2500 brain volume pairs*, with varying number of labeled anatomical regions and resolutions.

A natural way to evaluate whether two images are in a common coordinate frame is to evaluate the accuracy of overlap of gross morphological anatomical structures. The method considers measures of volume and surface overlap, volume similarity, and distance measures to evaluate the alignment of anatomical regions. Given a source label map  $S_r$  and target label map  $T_r$  and a cardinality operator  $|\cdot|$ , we consider the following overlap measures. We consider ‘target overlap’ and ‘mean overlap’ (also known as Dice score) as the primary measures of agreement between the source and target label maps.

$$TO_r = \frac{|S_r \cap T_r|}{|T_r|}, MO_r = 2 \frac{|S_r \cap T_r|}{|S_r| + |T_r|} \quad (1)$$

The aggregates over all regions are given by:

$$TO = \frac{1}{N_r} \sum_r TO_r, \quad MO = \frac{1}{N_r} \sum_r MO_r \quad (2)$$

To complement the above agreement measures, we also compute false negatives (FN), false positives (FP), and volume similarity (VS) coefficient for anatomical region  $r$ :

$$FN_r = \frac{|T_r \setminus S_r|}{|T_r|}, \quad FP_r = \frac{|S_r \setminus T_r|}{|S_r|}, \quad VS_r = 2 \frac{|S_r| - |T_r|}{|S_r| + |T_r|} \quad (3)$$

Comparison on other metrics proposed in <sup>29</sup> and regionwise analysis are shown in Figs. 11 and 12.

On the OASIS dataset, we use same the evaluation criteria as in the Learn2Reg challenge <sup>31</sup>, i.e. Dice score overlap and 95th percentile of the Hausdorff distance between 35 subcortical structures. This leads to a total of 12 evaluation metrics that we use to compare our method with 4 baselines - ANTs, Demons <sup>18</sup>, VoxelMorph <sup>32</sup> and SynthMorph <sup>33</sup>, representing established classical and deep learning registration algorithms.

**Lung CT mapping challenges** <sup>22,34</sup> Alignment of thoracic CT images, particularly the lungs and internal structures, is challenging due to their high deformability. Pulmonary registration has significant clinical applications, including aligning breath-hold scans for visual comparison, modeling lung expansion, and tracking disease progression. Murphy et al. introduced the EMPIRE10 challenge <sup>22</sup> to facilitate the evaluation of CT lung registration algorithms. The dataset comprises 30 scan pairs, including inspiration-expiration, breath-hold over time, 4D, ovine, contrast-noncontrast, and artificially warped scans. EMPIRE10 provides only scan pairs and binary lung masks, withholding fissures and landmarks for evaluation. The scans vary in spatial and physical resolution, necessitating a registration algorithm agnostic to anisotropy in both voxel and physical space. We use the challenge’s evaluation framework to assess fissure and landmark alignment and registration singularity. Our method is compared against two top performing methods – ANTs, which employs direct gradient descent, and DARTEL, which optimizes a stationary velocity field using server-reported metrics.

The National Lung Screening Trial (NLST) <sup>34</sup> subset curated by Learn2Reg challenge is another widely used community-standard dataset. It consists of 210 intra-subject lung pairs, with low-dose helical CT scans with limited field of view and high-dose scans with full field of view. The challenge provides more than thousand keypoints per subject pair, and we measure the Robust Target Registration Error (TRE30) in millimeters between the registered keypoints. We evaluate our method with a myriad of unsupervised methods, including ANTs <sup>13</sup>, VoxelMorph <sup>32</sup>, unigradICON <sup>35</sup> (with and without instance optimization), Vector-Field Attention <sup>36</sup>, Im2grid <sup>37</sup>, and RWC-Net <sup>38</sup>.

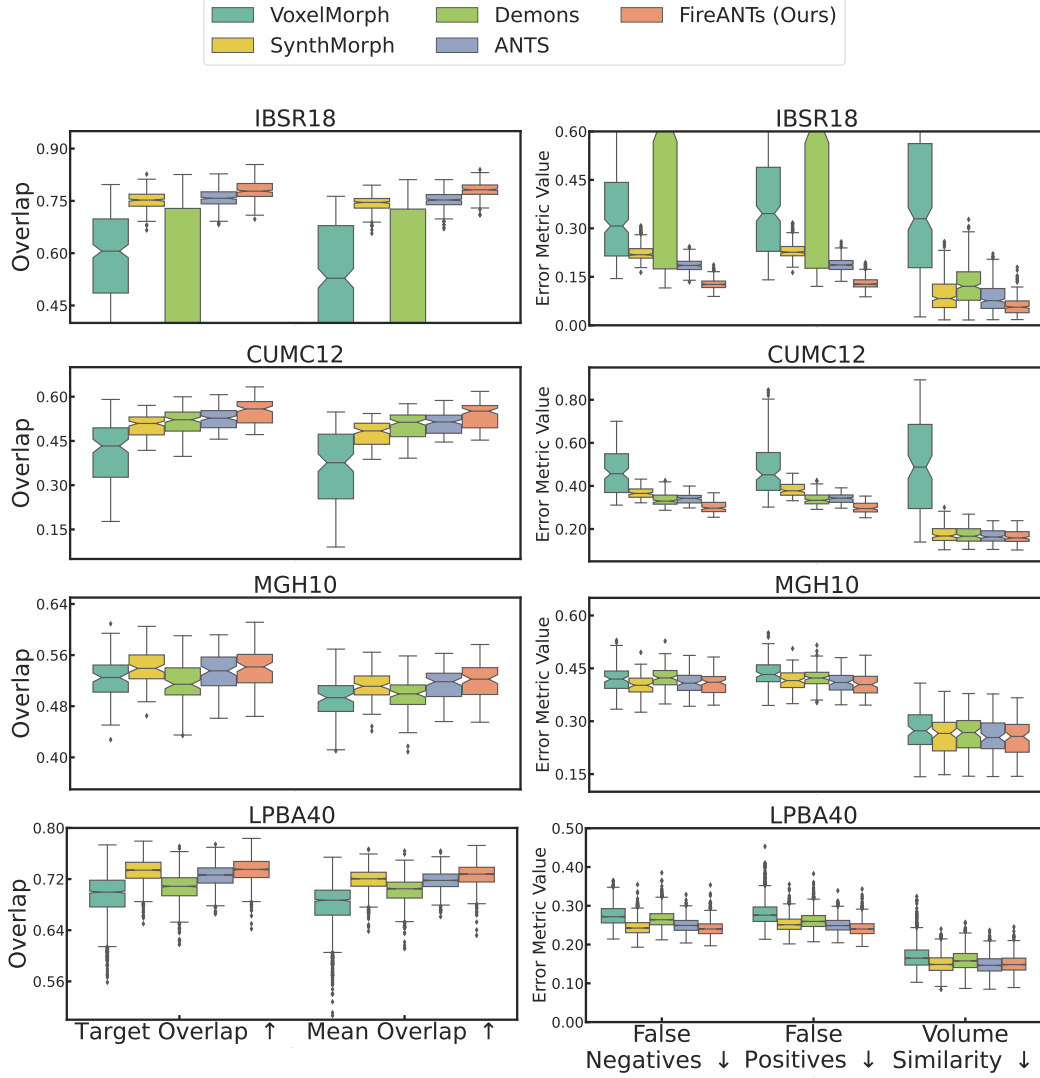


**Figure 1: FireANTs demonstrates state-of-the-art performance on Klein *et al.* challenge<sup>29</sup>:** Following the evaluation setup of Klein *et al.* paper, we validate registration performance using the average volume overlap of all anatomical label maps between the fixed and warped label maps. We consider ANTs (the winner of the challenge), and Diffeomorphic Demons as state-of-the-art optimization algorithms, and Voxelmorph and Synthmorph as state-of-the-art unsupervised deep learning baselines. Evaluation is shown for five metrics with  $\uparrow$  denoting a higher score is better, and  $\downarrow$  signifying a lower score is better. For deep learning baselines, appropriate preprocessing (intensity normalization, alignment, and resampling to 1mm isotropic) is performed to ensure a fair comparison, whereas no such preprocessing is required for optimization methods, including FireANTs. FireANTs shows significant gains in performance that are consistent across all four datasets, with the median overlap scores outperforming the third quartile of all other methods for IBSR18 and CUMC12 datasets. Comparison of overlap metrics by specific anatomical regions are in Fig. 11. For the overlap aggregation mentioned in <sup>29</sup>, results are shown in Fig. 12.

**RnR ExM Mouse Isocortex Dataset** <sup>39</sup> Expansion microscopy (ExM) is a fast-growing imaging technique for super-resolution fluorescence microscopy. The RnR-ExM challenge evaluates the ability to perform non linear deformable registration on ultra-high-resolution images. Out of the three species (mouse brain, *C. elegans*, zebrafish), the mouse isocortex dataset is the only dataset with non-trivial non-linear deformations. Registration of high-resolution sub-micron volumes is imperative to creating and understanding the comprehensive cell atlas of the mammalian brain at scale. The voxel size of each image volume is  $2048 \times 2048 \times 81$  and the voxel spacing is  $0.1625\mu\text{m} \times 0.1625\mu\text{m} \times 0.4\mu\text{m}$ . These volume sizes are about two orders of magnitude larger compared to existing biomedical datasets, representing a significant challenge in quick and scalable registration.

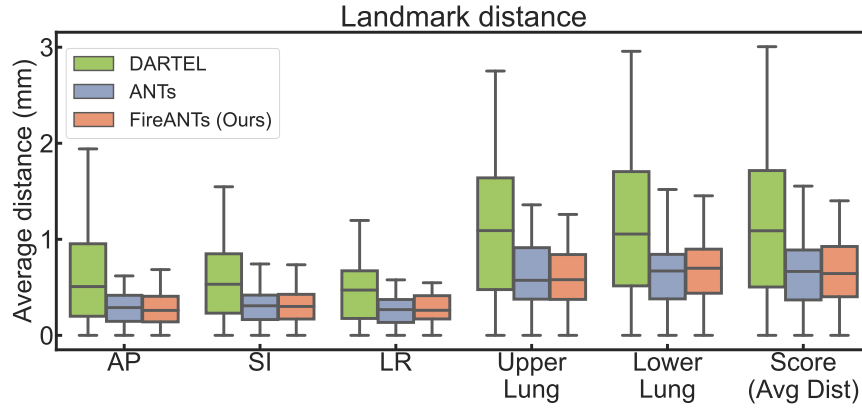
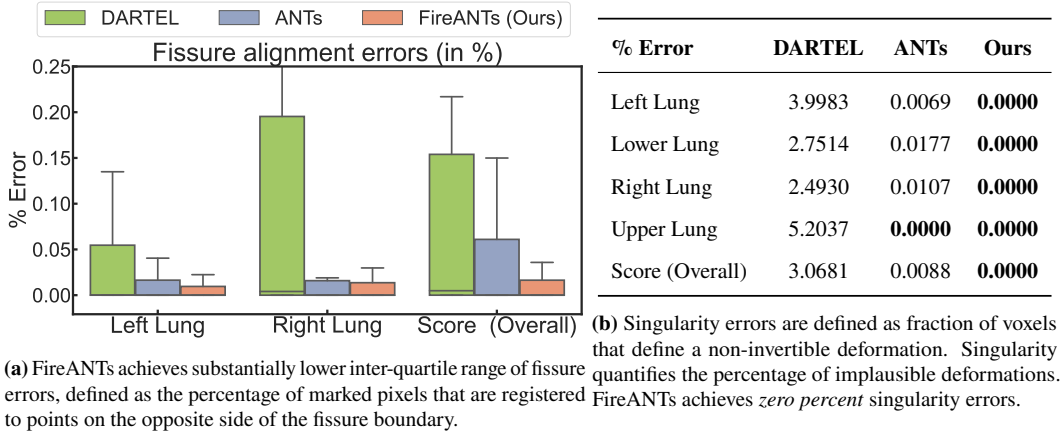
**BICCN Mouse Dataset** The high-throughput and high-resolution fluorescence micro-optical sectioning tomography (fMOST) platform<sup>40,41</sup> was used to image 55 mouse brains containing gene-defined neuron populations. The brains are imaged at a resolution of  $0.35 \times 0.35 \times 1.0\mu\text{m}^3$ . The dataset is used to generate a  $25\mu\text{m}$ -resolution atlas of the mouse brain in under 25 minutes. This unprecedented scale, enabled by FireANTs, will advance multimodal integration, standardize cross-species comparisons, and drive scalable, reproducible neuroscience research highly pertinent to large-scale collaborative efforts such as BICCN and BICAN.

## 2.2 Results on state-of-the-art biomedical benchmarks

**In-vivo brain MRI mapping** We compare FireANTs with two state-of-the-art optimization algorithms on Klein *et al.*<sup>29</sup>: ANTs - which won the original challenge, and Symmetric Log Demons<sup>18</sup>, and two widely used deep learning algorithms: VoxelMorph<sup>32</sup> and SynthMorph<sup>33</sup> using their provided pretrained models. For all the four datasets, we first fit an affine transformation from the moving image to the fixed image, followed by a diffeomorphic transform. For the OASIS dataset, all images are already affine-aligned to the MNI atlas. Since no methods utilize label maps, we run registration on all 414 image pairs prescribed in the dataset. Results for the brain datasets are shown in Fig. 1, Fig. 11, and Table 1.

Our algorithm outperforms all baselines on four out of five datasets, with an improvement in *all* metrics evaluating the volume overlap of the fixed and warped label maps. The improvements are consistent across varying parcellations and relative sizes of anatomical label maps. In the IBSR18 and CUMC12 datasets, the median target overlap of our method is better than the third-quantile of ANTs. Fig. 11 also highlights the improvement in label overlap per labeled brain region across all datasets. For deep methods, a noticeable performance drop is observed when the anisotropic volumes are fed into the network, which is undesirable as the trained model is essentially ‘locked’ to a single physical resolution - which limits the generalizability of the model to various modalities with different physical resolutions. For Demons, ANTs, and FireANTs (Ours), we do not perform any additional normalization or resampling. On the OASIS dataset, all methods perform at par with each other with no significant differences. SynthMorph is more robust to the domain gap than VoxelMorph due to its training strategy with synthetic images, but still underperforms optimization baselines when their recommended hyperparameters are chosen.

### Lung CT mapping challenges



Method	Left Lung	Right Lung	Score (% Error Overall)
FireANTs (Ours)	0.0185	0.0254	0.0227
MRF Correspondence Fields	0.0824	0.0211	0.0485
ANTs	0.0249	0.1016	0.0747
Dense Displacement Sampling	0.0578	0.0919	0.0826
ANTs + BSpline	0.0821	0.0848	0.0861
DISCO	0.1256	0.0499	0.0882
VIRNet	0.0834	0.0934	0.0890
Feature-constrained nonlinear registration	0.1210	0.0758	0.1032
Explicit Boundary Alignment	0.1063	0.1246	0.1209
MetaReg	0.1049	0.2224	0.1791

(d) Fissure alignment error on top 10 algorithms in the challenge sorted by fissure alignment error, averaged on all scan pairs. FireANTs outperforms state-of-the-art algorithms highlights the forms a wide array of baselines, including direct optimization (ANTs, effective performance of FireANTs on the NLST ANTs+BSpline), neural networks (VIRNet), and explicit correlation vol- dataset, outperforming a plethora of state-of-the-art umes (MRF, Disco).

**Figure 2: FireANTs demonstrates state-of-the-art performance on community-standard lung CT challenges:** (a) **EMPIRE10:** Lung fissure plates are an important anatomical landmark demarcating lobes within the lung. Fissure alignment errors (in %) denote the percentage of locations near the lung fissure plates that are on the wrong side of the fissure post-registration. Over all 30 scan pairs, our method performs 5× better than ANTs. (b) **EMPIRE10:** Singularity errors defined as percentage of voxels that have a non-diffeomorphic deformation, a proxy for physically implausible deformations. In the DARTel baseline, singularities can be introduced for larger deformations due to numerical approximations of the integration. Even for ANTs, the solutions (deformations) returned are not entirely diffeomorphic. Our method shows much better fissure and landmark alignment (Fig. 2(a,c), Fig. 14, Fig. 15) with guaranteed diffeomorphic transforms. (c) **EMPIRE10:** Landmark distance in mm for selected landmarks. Across different lung subregions, our method shows results at least at par with ANTs, with slightly better average and median results across all regions. (d) **EMPIRE10:** Shows the top 10 algorithms for average fissure alignment error in % in the EMPIRE10 challenge. Error metrics are taken from the evaluation server. Other methods perform well on one lung (MRF for right, ANTs for left) but comparatively poorly on the other lung, compared to our method showing both accurate and robustness to both the left and right lung. (e) **NLST:** Landmark distance in mm for provided landmarks. Our method outperforms a variety of state-of-the-art optimization and deep learning algorithms.

**EMPIRE10** : The EMPIRE10 lung images represent volumes that are about  $10\times$  larger than the brain dataset, thereby presenting a scaling challenge for deformable registration algorithms. We evaluate three criteria: (1) fissure alignment errors (%)—the fraction of misaligned fissure voxels (Figs. 2a and 2d), (2) landmark distance in mm (Fig. 2c), and (3) singularity errors—the fraction of non-diffeomorphic voxels (Fig. 2b). Fig. 2 highlights the impact of representation choice in modeling diffeomorphisms. DARTEL, using an exponential map, performs significantly worse than ANTs across all metrics by three orders of magnitude. In contrast, our method reduces fissure alignment error by  $5\times$  compared to ANTs and outperforms it in 5 out of 6 landmark subregions. While all methods theoretically ensure diffeomorphism, SVF-based approaches introduce singularity errors due to non-adaptive scaling-and-squaring. ANTs also introduces some singularities, whereas our method computes numerically perfect diffeomorphic transforms. Finally, Fig. 2d compares fissure alignment errors among EMPIRE10 submissions, showing FireANTs achieves the lowest landmark errors and the fastest runtime among the top 10 methods, setting new benchmarks in computational efficiency and accuracy.

**NLST**: For the NLST dataset, we compare with many representative state-of-the-art algorithms, both based on optimization and deep-learning. We use the evaluation criteria provided by the challenge, and measure results on the Robust Target Registration Error (TRE30) in millimeters between the registered keypoints. Results in Fig. 2e show that FireANTs outperforms all baselines on the NLST dataset, with improvements of upto 51.6% in robust target registration error (TRE30) of provided keypoints compared to state-of-the-art deep learning benchmarks including Im2Grid, Vector-Field Attention, RWC-Net, and a 50.8% improvement in TRE30 over foundation models like unigradICON. This demonstrates the broad applicability of FireANTs beyond neuroimaging applications.

### 2.3 Evaluation on high-resolution mouse isocortex registration

Expansion Microscopy (ExM) is an emerging super-resolution fluorescence imaging technique that enables 3D nanoscale visualization of cellular and molecular structures<sup>42</sup>. While ExM provides rich structural data, its large-scale images remain challenging for existing registration algorithms due to repetitive textures, highly non-linear hydrogel deformations, imaging noise, and size constraints. The Robust Non-rigid Registration Challenge for Expansion Microscopy (RnR-ExM)<sup>39</sup> offers a benchmark dataset, where we focus on registering mouse isocortex images, characterized by hydrogel-induced deformations and staining intensity loss. Each volume ( $2048 \times 2048 \times 81$  voxels) has a voxel spacing of  $0.1625\mu m \times 0.1625\mu m \times 0.4\mu m$  and is 40.5 times larger than brain imaging datasets. Current state-of-the-art methods either register small independent chunks<sup>43</sup>, losing inter-chunk information, or process highly downsampled images<sup>44</sup>, significantly reducing resolution (by  $64\times$  in-plane).

In contrast, FireANTs is able to register the volume at native resolution. We perform an affine registration followed by a diffeomorphic registration step. The entire method takes about 2-3 minutes on a single A6000 GPU. As shown in Fig. 3, our method secures the first place on the leaderboard, with a considerable improvement in the Dice score and a  $4.42\times$  reduction in the standard deviation of the Dice scores compared to the next best method. Fig. 3 also shows qualitative comparison of our method compared to Bigstream<sup>43</sup>, the winner of the RnR-ExM challenge. Bigstream only performs an affine registration, leading to inaccurate registration in one of three test volumes, leading to a lower average Dice score and higher variance. Moreover, the affine registration leads to boundary in-plane slices being knocked out of the volume, leading to poor registration (Fig. 3). FireANTs preserves the

boundary in-plane slices during its affine step, and subsequently performs an accurate diffeomorphic registration. This shows the versatility and applicability of FireANTs for high-resolution microscopy registration.

## 2.4 Ease of experimentation due to efficient implementation

One of the major contributions of our work is to enable fast and scalable image registration while improving accuracy. In applications like atlas/template building, registration is used in an iterative manner (in the ‘inner loop’) of the optimization. Another application that requires fast runtimes is hyperparameter tuning, since different datasets and modalities admit notably different hyperparameters for optimal registration. This calls for an rapidly escalating need for fast and scalable registration algorithms. Although in theory CPUs can scale with more cores, the cost per TFLOP is significantly higher than GPUs. Moreover, we note that beyond 16 threads, ANTs does not show any significant speedup due to parallelization overheads, limiting its scalability even on high-end servers.

To demonstrate the computational and runtime efficiency of our method, we demonstrate the runtime of our library on the brain and lung benchmarks. All the experiments for our method are run on a single A6000 GPU, with a batch size of 1, to avoid amortizing runtime over a bigger batch size. In practice, higher speedups can be obtained by registering batches of images that fit in a single GPU. For the brain datasets, we run ANTs with the recommended configuration with AMD EPYC 7713 Processor (single thread) and 512GB RAM. For the EMPIRE10 lung dataset, we use the runtimes described in the writeup provided as part of the challenge. A runtime analysis of our method on the brain and EMPIRE10 datasets are shown in Fig. 4.

**FireANTs is up to three orders of magnitude faster than ANTs** For the EMPIRE10 dataset, we compare our method with both ANTs and DARTEL implementations. We capture the runtime for each scan pair and aggregate the average, minimum and maximum runtimes and speedups in Fig. 4b. FireANTs reduces the runtime from 1 to 12 hours for a single scan pair to *under a minute*. Since the exponential map requires a few integration steps for each iteration and pullback of the gradient from the warp to the velocity field, this variant is significantly slower than ANTs. In contrast, our method achieves a *minimum* of more than  $300\times$  speedup over ANTs, while maintaining high accuracy. In the brain datasets, our method achieves a consistent speedup of three orders of magnitude. This occurs due to a better choice of hyperparameters compared to the baseline, faster convergence due to the adaptive optimization, and better memory and compute utilization by efficient cuDNN implementations.

On the brain datasets, we compare our method with ANTs, and compute the runtime and speedups for each scan pair. We then plot a histogram of the speedup and aggregate the runtime and speedup in Fig. 4a. On all datasets, the average speedup is over  $1000\times$ , signifying a new paradigm for image registration workflows. These improvements in runtime occur while also providing at par, or superior quantitative and qualitative results (Fig. 1, 2, Extended Data 14, 15).

**FireANTs enables rapid prototyping and hyperparameter tuning** In optimization toolkits such as ANTs, correct choice of hyperparameters are key to high quality registration. Some of these hyperparameters are the window size for the similarity metric Cross-Correlation or bin size for Mutual Information. In our experience, the Gaussian smoothing kernel  $\sigma_{\text{grad}}$ ,  $\sigma_{\text{warp}}$  for the gradient

(a) Snapshot of the RnR-ExM leaderboard

#	↑	User (Team)	Created	DSC
1st		rohit.rango ✓	11 Aug. 2023	$0.92049045 \pm 0.00996840$
2nd		rohit.rango ✓	17 Aug. 2023	$0.91875541 \pm 0.01803930$
3rd		cwmokab ✓ (Orange)	15 March 2023	$0.91688563 \pm 0.04410269$
4th		cwmokab ✓ (Orange)	12 March 2023	$0.91544257 \pm 0.04463970$
5th		NLI10Me ✓ (bigstream)	14 March 2023	$0.91426871 \pm 0.03391914$
6th		acasamitjana ✓	23 June 2023	$0.91321484 \pm 0.02358535$
7th		NLI10Me ✓ (bigstream)	14 March 2023	$0.91209382 \pm 0.03194342$
8th		cwmokab ✓ (Orange)	15 March 2023	$0.91111042 \pm 0.04326616$
9th		NLI10Me ✓ (bigstream)	14 March 2023	$0.90968117 \pm 0.02988877$
10th		xi	15 March 2023	$0.90895331 \pm 0.03555638$

(b) Qualitative comparison of registration of Bigstream and FireANTs

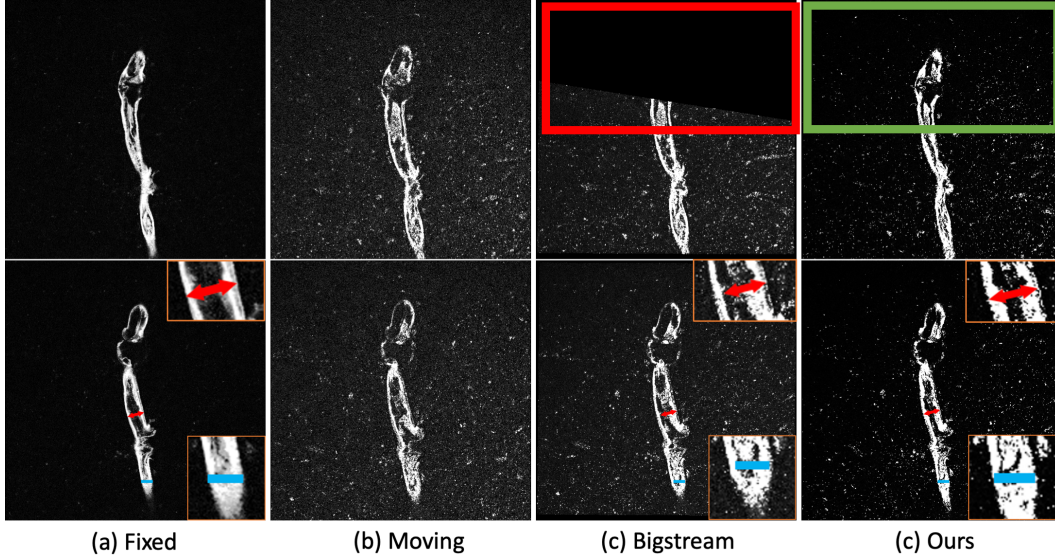
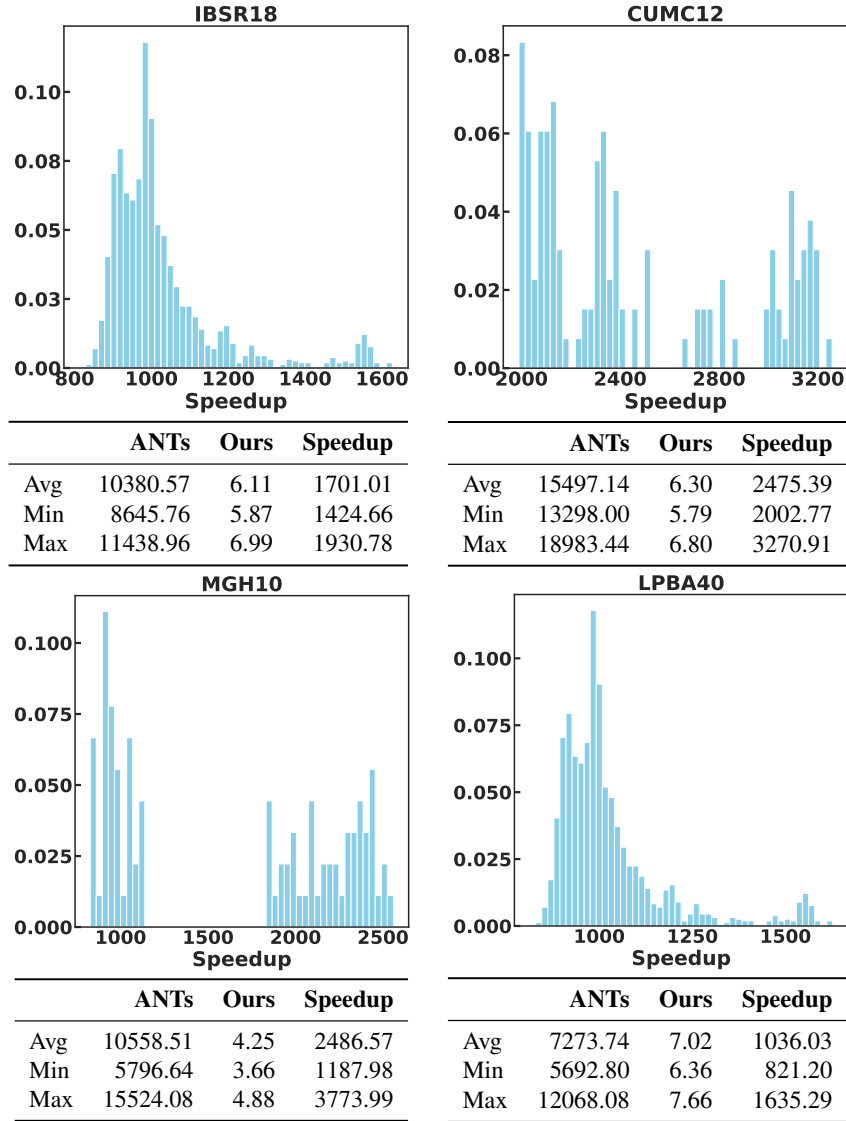


**Figure 3: FireANTs secures first rank in the RnR-ExM mouse dataset:** (a): As of May 6, 2025, our method ranks first in the mouse brain registration task, which is the only task in the challenge requiring deformable registration. Our top two successful submissions secure the first and second position, with a 0.361 improvement in Dice score compared to the 3rd ranked submission, which is 0.261 better than the 5th ranked submission (bigstream). Note that among the top 10 submissions, our method has the lowest standard deviation ( $4.42\times$  lower than the second best submission) showing the robustness of our model across different microscopy volumes. (b) shows a qualitative comparison of FireANTs with Bigstream<sup>43</sup>, the other top leading method in the challenge. The moving image volumes have substantially more noise than the fixed image volumes, making intensity-based registration difficult. The non-rigid deformation dynamics of the hydrogel are clearly visible, as the moving volume has a thicker boundary than the fixed volume. Bigstream does not capture these dynamics very well – this is illustrated by comparing the thickness of the cortex at various points (zoomed orange crops in bottom row), where Bigstream does not deform the cortex enough to match the fixed image. FireANTs deforms and accurately depicts these morphological changes, which can be crucial for downstream morphometric studies. Moreover, the affine registration in Bigstream knocks the boundary slices out of the volume (red highlight in top row), leading to drop in registration performance. On contrary, our method’s affine and deformable stages are more stable, leading to better registration and avoiding spurious out-of-bound artifacts at the boundary slices.

(a) Histogram and summary of runtime on four brain MRI datasets.



(b) Runtime analysis and summary on EMPIRE10 dataset

	ANTs	DARTEL	Ours	Speedup (ANTs)	Speedup (DARTEL)
Avg	6hr 14m	7hr 16m	0m 39s	562.67	663.77
Min	0h 55m	1h 8m	0m 9s	320.74	315.23
Max	12h 41m	10h 11m	1m 5s	1231.27	796.51

**Figure 4: FireANTs facilitates quick and scalable registrations.** We compare the runtime of our implementation with the ANTs library. (a) shows histogram of speedup (runtime of ANTs divided by runtime of our method) and statistics of runtimes (in seconds) for the four brain MRI datasets. For all datasets, our implementation runs a *minimum* of two orders of magnitudes faster, making it suitable for hyperparameter search algorithms, and larger datasets. Table (b) shows the runtime of ANTs, DARTEL and our implementation on the EMPIRE10 challenge data. The first three columns show the actual runtime of the methods, followed by the speedup obtained by our method when compared to ANTs and DARTEL. Note that our method runs a *minimum* of 320 times faster than ANTs, saving a substantial amount of time, at no loss in registration quality.

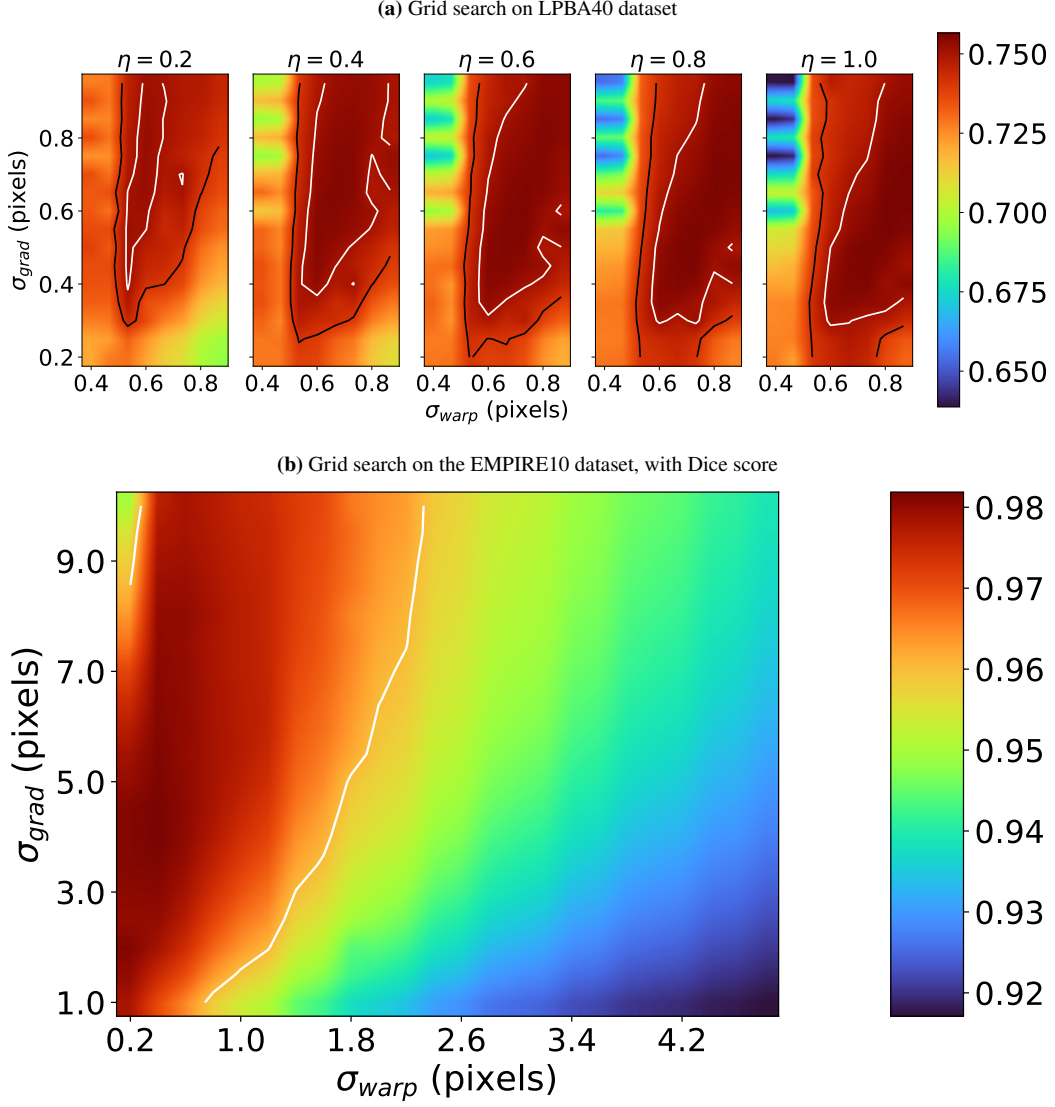


**Figure 5: FireANTs facilitates feasibility of extensive hyperparameter search in registration** The speed of FireANTs makes hyperparameter studies like these feasible, which ANTs would take years to complete. (a): We perform a hyperparameter grid search on three hyperparameters of interest - smoothing kernel for the warp field ( $\sigma_{\text{warp}}$ ) in pixels, smoothing kernel for the gradient of warp field ( $\sigma_{\text{grad}}$ ) in pixels and learning rate  $\eta$ . The metric to optimize in this case is the target overlap. For the LPBA40 dataset, we perform a hyperparameter sweep over 640 configurations in 40 hours with 8 A6000 GPUs. A corresponding hyperparameter sweep with 8 concurrent jobs with each job consuming 8 CPUs would take  $\sim 3.6$  years to complete. The white contour representing the level set for target overlap = 0.75, and the black contour representing the level set for target overlap of 0.74 show the robustness of our method to hyperparameters - performance is not brittle or sensitive to choice of hyperparameters. (b): Hyperparameter grid search on the EMPIRE10 dataset over  $\sigma_{\text{warp}}$  and  $\sigma_{\text{grad}}$  parameters (456 configurations), with a fixed learning rate of  $\eta = 0.25$ . The metric to optimize is the Dice score of the provided binary lung mask. This sweep takes about 12.37 hours on 8 GPUs, whereas a corresponding sweep would take 296 days for ANTs and 345 days for DARTEL (more in Fig. 4). The white contour corresponds to the level set for Dice score = 0.96, showing both a huge spectrum of parameters that achieve high Dice scores, and low sensitivity of the method to choice of hyperparameters.

and the warp field are two of the most important parameters for accurate diffeomorphic registration. The optimal values of these hyperparameters vary by image modality, intensity profile, noise and resolution. Typically, these values are provided by some combination of expertise of domain experts and trial-and-error. However, non experts may not be able to adopt these parameters in different domains or novel acquisition settings. Recently, techniques such as hyperparameter tuning have become popular, especially in deep learning.

In the case of registration, hyperparameter search can be performed by considering some form of label/landmark overlap measure between images in a validation set. We demonstrate the stability and runtime efficiency of our method using two experiments : (1) Owing to the fast runtimes of our implementation, we show that hyperparameter tuning is now feasible for different datasets. The optimal set of hyperparameters is dependent on the dataset and image statistics, as shown in the LPBA40 and EMPIRE10 datasets; (2) within a particular dataset, the sensitivity of our method around the optimal hyperparameters is very low, demonstrating the robustness and reliability of our method. We choose the LPBA40 dataset among the 4 brain datasets due to its larger size ( $40 \times 39 = 1560$  pairs). We choose three parameters to search over : the learning rate ( $\eta$ ), and the gaussian smoothing parameters  $\sigma_{\text{warp}}, \sigma_{\text{grad}}$ . We use the Ray library (<https://docs.ray.io/>) to perform a hyperparameter tuning using grid search. For the LPBA40 dataset, a grid search over three parameters (shown in Fig. 5a) takes about 40.4 hours with 8 parallel jobs. On the contrary, ANTs would require around 3.6 years to complete the same grid search, with 8 threads allocated to each job and 8 parallel jobs. This makes hyperparameter search for an unknown modality computationally tractable. Fig. 5a shows a dense red region suggesting the final target overlap is not sensitive to the choice of hyperparameters. Specifically, the maximum target overlap is 0.7565 and 58.4% of these configurations have an average target overlap of  $\geq 0.74$ . This is demonstrated in Fig. 5a by the white contour line denoting the level set for target overlap = 0.75, and the black contour line denoting the level set for target overlap of 0.74. The target overlap is quite insensitive to the learning rate ( $\geq 0.4$ ) showing that our algorithm achieves fast convergence with a smaller learning rate. On the EMPIRE10 dataset, we fix the learning rate and perform a similar hyperparameter search over two parameters, the Gaussian smoothing parameters  $\sigma_{\text{warp}}, \sigma_{\text{grad}}$ , shown in Fig. 5b. We use the average Dice score between the fixed and moving lung mask to choose the optimal hyperparameters. FireANTs can perform a full grid search over 456 configurations on the EMPIRE10 dataset in 12.37 hours with 8 A6000 GPUs, while it takes SyN 10.031 days to run over a single configuration. Normalizing for 8 concurrent jobs and 456 configurations, it would take ANTs about 296 days, and DARTEL about 345 days. This shows that our method and accompanying implementation can now make hyperparameter search for 3D image registration studies feasible.

## 2.5 FireANTs facilitates scalable atlas generation

Atlas generation is an important component of integrating large-scale imaging data – including gene expression, connectivity patterns, and functional properties — onto a common spatial coordinate system facilitating multimodal data alignment and comparison. This requires atlas (or template) generation capabilities that scale with the unprecedented scale of acquired data. In this section, we showcase the efficiency of atlas generation by reproducing the fMOST atlas proposed in the ANTsX ecosystem<sup>45</sup> for the mouse brain. We follow the steps outlined in the ANTsX Ecosystem<sup>45</sup> for generating an fMOST atlas of the mouse brain, including preprocessing steps like downsampling

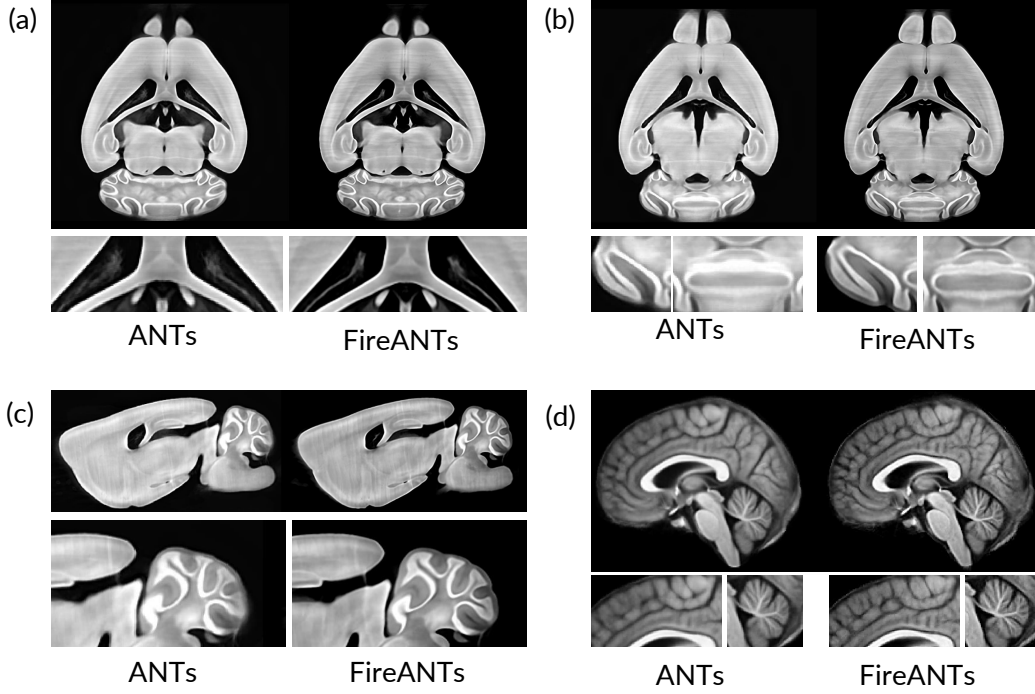


**Figure 6:** Comparison of brain templates (atlases) constructed using ANTs (left) and FireANTs (right). **(a–c)** Coronal and sagittal sections of the 25 $\mu$ m fMOST mouse brain template illustrate the improved structural fidelity of FireANTs. In the ANTs template, the internal regions of the lateral ventricles appear blurred (a), and the cerebellar architecture exhibits intensity bleeding (b, c), whereas FireANTs yields crisper delineation of these anatomical structures. **(d)** The in vivo human brain atlas further demonstrates the advantages of FireANTs, with sharper cortical folding and improved contrast and realistic intensity features in the cerebellum compared to ANTs. FireANTs generates multiple high-fidelity templates while being 200-400 times faster than ANTs.

to 25 $\mu$ m resolution, destriping, flipping along the sagittal plane for left-right symmetry, bias field correction, and affine preregistration to a common template. Since no parcellations are available for the dataset, we qualitatively compare the atlases generated by ANTs and FireANTs, and compare their runtimes. We also generate an in-vivo atlas for the OASIS dataset, to show scalability on smaller datasets and for quantitative evaluation. Fig. 6 shows that the atlas generated by both methods is similar in terms of quality. On a 64-thread core machine, ANTs takes 141.5 hours to generate the atlas with 6 epochs of template refinement. With the identical number of iterations and configuration, FireANTs runs in 22 minutes with a distributed setup on an 8-GPU workstation, showing a significant improvement in runtime efficiency. On a much lower-resolution OASIS dataset, ANTs takes 2 hours and 16 minutes to generate an atlas with 16 subjects, while FireANTs runs in 32 seconds. To quantify atlas fidelity, we evaluate Dice Score overlap of image pairs after registering them to the atlas. While pairwise Dice score overlap of subjects is  $0.704 \pm 0.163$  with the ANTs template, the FireANTs template improves the Dice score to  $0.722 \pm 0.161$ . This demonstrates that FireANTs can be used to generate high-fidelity atlases two orders of magnitude faster than ANTs at no loss in image quality,

making it a powerful tool for large-scale atlas generation.

## 2.6 Independent Evaluation

Since the release of our code and documentation, FireANTs has been independently adopted by researchers in the field. Few anecdotal examples include the registration of high-resolution histology slides, and non-human primate data <sup>46,47</sup>. A compelling independent application and evaluation is performed by NextBrain <sup>48</sup>, a tool that utilizes FireANTs to perform Bayesian segmentation of in-vivo and ex-vivo brain MRI scans. NextBrain uses FireANTs to register input brain MRI scans to an augmented template with a resolution of  $200\mu m$  and 333 regions of interest, providing a comprehensive structural analysis of the subject. Quantitatively, incorporating FireANTs in the pipeline leads to no loss in performance as measured by Dice overlap. The utilization of GPU-based toolkits including FireANTs reduces the runtime from 2-3 days / one week for  $1mm$  in-vivo /  $300\mu m$  ex-vivo scans on a multi-core workstation, to *less than 5 minutes* on a GPU. This demonstrates the accessibility, scalability and efficiency of FireANTs in real-world applications.

## 3 Discussion

We present FireANTs, a powerful and general-purpose multi-scale registration algorithm. Our method performs registration by generalizing the concept of first-order adaptive optimization schemes for optimizing parameters in a fixed Euclidean space, to multi-scale *diffeomorphisms*. This generalization is highly non-trivial because diffeomorphisms are typically implemented as an image grid proportional to the size of the fixed image, and are optimized in a multi-scale manner to capture large deformations <sup>13,17,49</sup> leading to changing grid size throughout optimization. Our method also avoids computationally expensive parallel transport and riemannian metric tensor computation steps for diffeomorphisms by solving an Eulerian descent that exploits the group structure to define descent directions from the identity transform. FireANTs achieves consistent improvements in performance over state-of-the-art optimization-based registration algorithms like ANTs, DARTEL, SynthMorph and Bigstream. This improvement is shown across six datasets with a spectrum of anatomies (in-vivo human brain, human, ovine and synthetic lungs, mouse isocortex and mouse brain), contrast, image volume sizes (ranging from 196 up to 2048 voxels per dimension), and modalities (MRI, CT, microscopy, sectioning tomography). A key advantage of our method is that *we do not tradeoff* any of accuracy, speed, or robustness for the others, thus being a powerful registration algorithm.

Our method shows consistent improvements and robust performance on five community reference brain MRI datasets. Researchers have developed numerous classical image registration methods specifically for neuroimaging studies <sup>13,17,50,51</sup> but registration remains an open challenge in brain mapping <sup>52,53</sup>. FireANTs' consistent improvement in performance can be attributed to the quasi-second-order update, which normalizes the varying curvature of per-pixel gradients, leading to faster convergence and better local minima. This performance is consistent across metrics (Fig. 1) and anatomical structures (Fig. 11). With the acquisition of larger datasets <sup>30</sup> and high-resolution imaging <sup>27,39,54</sup> owing to rapidly growing image acquisition technology and innovations, fast runtime and accurate registration become imperative to enable large-scale studies. Our performance comes with a reduction of runtime of up to three orders of magnitude on standard datasets.

We also demonstrate competitive performance in the EMPIRE10 and NLST challenges, widely regarded as a comprehensive evaluation of registration algorithms<sup>31,55</sup> for lung CT images. Unlike the brain imaging datasets, the EMPIRE10 dataset contains images with large deformations, anisotropic image spacings and voxel sizes, thin structures like airways and pulmonary fissures, which are hard to align based on image intensity alone. These image volumes are typically much larger than what deep learning methods can currently handle at native resolution<sup>32,44,55</sup>. FireANTs performs much better registration in terms of landmark, fissure alignment, and singularities, while being two orders of magnitude faster than existing state-of-the-art. This experiment also calls attention to a much-overlooked detail - the performance gap due to the choice of representation of diffeomorphisms (direct optimization versus exponential map). We show that direct optimization of the group element is preferable to exponential maps, both in FireANTs and in baselines (ANTs versus DARTEL). This improvement can be attributed to the representation - one can interpret direct optimization as integrating a set of *time-dependent* velocity fields since the gradients change throughout optimization, allowing more flexibility in the space of diffeomorphisms it can represent, whereas SVF performs the integral of a *time-independent* velocity field by design. Moreover, computing the exponential map is expensive for diffeomorphisms since the number of iterations can be higher for larger deformations<sup>17</sup>. For example, in Fig. 4(a), the exponential map representation (DARTEL) takes substantially longer to run than ANTs. Shooting methods modify the velocity field at each iteration and tend to be sensitive to hyper-parameter choices. For example, in Fig. 2, the results for shooting methods are substantially worse than for methods that optimize the transformation directly. We also observe this for the LPBA40 dataset in Fig. 16, where the shooting method consistently underperformed over a wide range of hyperparameter choices.

FireANTs is consistently  $300\text{--}2000\times$  faster than existing CPU-based state-of-the-art, is robust to the choice of hyperparameters, allowing users to utilize principled hyperparameter search algorithms for novel applications or modalities. This speedup is also shown by generating an in-vivo human brain atlas in  $\sim 30$  seconds, and a  $25\mu m$  mouse brain atlas in less than 25 minutes. This quick runtime will enable fast and accurate registration of high-resolution mesoscale and microscale imaging data that will play a paramount role in advancing our understanding of connectomics, neuroscience, cellular and molecular biology, genetics, pathology, among many other disciplines in the biomedical and biological sciences. With breakthrough advances in high-resolution, high-throughput imaging techniques, it is imperative for registration algorithms to also scale with the inordinate amounts of data. In summary, FireANTs is a powerful and general-purpose multi-scale registration algorithm and sets a new state-of-the-art benchmark. We propose to leverage the accurate, robust, and fast library to speed up registration workflows for ever-growing needs of performant and fast image registration in a spectrum of disciplines within the biomedical and biological sciences, wherein algorithms are bottlenecked by scalability.

## 4 Methods

### 4.1 Preliminaries

Given  $d$ -dimensional images  $I : \Omega \rightarrow \mathbb{R}^d$  and  $I' : \Omega \rightarrow \mathbb{R}^d$  where the domain  $\Omega$  is a compact subset of  $\mathbb{R}^2$  or  $\mathbb{R}^3$ , image registration is formulated as an optimization problem to find a transformation

$\varphi$  that warps  $I'$  to  $I$ . The transformation can belong to an algebraic group, say  $G$ , whose elements  $g \in G$  act on the image by transforming the domain as  $(I \circ g)(x) = I(g(x))$  for all  $x \in \Omega$ . The registration problem solves for

$$\varphi^* = \underset{\varphi \in G}{\operatorname{argmin}} L(\varphi) \doteq C(I, I' \circ \varphi) + R(\varphi) \quad (4)$$

where  $C$  is a cost function, e.g., that matches the pixel intensities of the warped image with those of the fixed image, or local normalized cross-correlation or mutual information of image patches. There are many types of regularizers  $R$  used in practice, e.g., total variation, elastic regularization<sup>56</sup>, enforcing the transformation to be invertible<sup>57</sup>, or volume-preserving<sup>58</sup> using constraints on the determinant of the Jacobian of  $\varphi$ , etc. If, in addition to the pixel intensities, one also has access to label maps or different anatomical regions marked with correspondences across the two images, the cost  $C$  can be modified to ensure that  $\varphi$  transforms these label maps or landmarks appropriately.

#### 4.1.1 Properties of the considered Transformation Group

A diffeomorphism is a smooth and invertible map with a corresponding differentiable inverse map<sup>59–61</sup>. We denote the set of all diffeomorphisms on  $\Omega$  as  $\operatorname{Diff}(\Omega; \mathbb{R}^d)$ . It is useful to note that unlike rigid or affine transforms that have a fixed number of parameters, diffeomorphisms require dense and variable parameterization, typically proportional to the size of the image. When groups of transformations on continuous domains are endowed with a differentiable structure, they are called Lie groups. Diffeomorphisms are also examples of Riemannian manifolds, and are amenable to Riemannian optimization (see §4.3.2).

In this work, we only consider a subgroup of diffeomorphisms. Consider the set of continuously differentiable functions  $u \in C_0^1(\Omega, \mathbb{R}^d)$  such that  $u, J(u) = 0$  on  $\partial\Omega$ , where  $J(u)$  is the Jacobian of  $u$ , such that  $[J(u)(x)]_{ij} = \frac{\partial u(x)_i}{\partial x_j}$ . These functions can be extended to have  $u \equiv 0$  outside  $\Omega$ . Then, for a small enough  $\epsilon > 0$ ,  $x + \epsilon u(x)$  is a diffeomorphism (Proof in Proposition 8.6 in<sup>61</sup>). Although these diffeomorphisms are close to identity, diffeomorphisms with larger deviations from the identity can be constructed by composing these ‘small diffeomorphisms’. Therefore, we study the subgroup of diffeomorphisms of the form

$$\phi_n = (id + \epsilon_1 u_1) \circ \dots \circ (id + \epsilon_n u_n) \quad (5)$$

where  $u_i$ s are defined as before. We denote this subgroup as  $G(\Omega, \mathbb{R}^d)$ . This subgroup retains the group structure with identity element  $id$ , the composition operation  $\circ$  induced from  $\operatorname{Diff}(\Omega, \mathbb{R}^d)$ , and the inverse group element:  $\phi_n^{(-1)} = (id + \epsilon_n u_n)^{(-1)} \circ \dots \circ (id + \epsilon_1 u_1)^{(-1)}$  (as each individual  $id + \epsilon_n u_n$  is shown to have an inverse<sup>61</sup>). The elements of this subgroup can be thought of as diffeomorphisms arising from time-varying continuously differentiable flows.

However, the rate of convergence of these algorithms are contingent on the severity of ill-conditioning of (4). In subsequent sections, we first show the extent of ill-conditioning for diffeomorphic registration which subsequently warrants adaptive optimization over this subgroup of diffeomorphisms.

## 4.2 Deformable Image Registration is a severely ill-conditioned problem

The ill-conditioned nature of image registration represents a comparatively neglected domain of inquiry within the extant literature. Recent works in the literature <sup>62,63</sup> only speculate the ill-conditioned nature of registration but do not quantify it. Computing the ill-conditioning requires us to analyze the Hessian of the registration cost function. This is infeasible in general due to the high dimensionality of the problem; the full Hessian of a MRI brain registration problem requires more than 15 petabytes of memory to store. However, we consider a typical scenario of T1-weighted 3D MRI image registration with the L2 loss <sup>15,16,32</sup>: i.e.  $C(I_f, I_m, \varphi) = \sum_i (I_f(\mathbf{x}_i) - I_m(\varphi(\mathbf{x}_i)))^2$ . In this case, the gradient of  $C$  w.r.t.  $\varphi(\mathbf{x}_i)$  is  $(I_m(\varphi(\mathbf{x}_i)) - I_f(\mathbf{x}_i)) \nabla I_m(\varphi(\mathbf{x}_i))$ , which does not depend on  $\varphi(\mathbf{x}_j), j \neq i$ . Therefore, the full Hessian is simply a block-diagonal matrix containing pixelwise Hessians  $H_i = \nabla_{\varphi(\mathbf{x}_i)}^2 C$  with eigenvalues  $\{\lambda_i; i = \{1, 2, 3\}\}$ . This makes the conditioning analysis tractable. We calculate the per-pixel condition number, defined as  $\kappa_i = |\lambda_i^{\max}|/|\lambda_i^{\min}|$ ; and investigate the relationship between the fraction of foreground pixels and  $\kappa_i$  across multiple spatial resolutions of the images. The study considers three downsampling factors: 1x (original resolution), 2x, and 4x, in accordance with existing multi-scale optimization techniques. Fig. 8 shows that across all resolutions, more than 60% of foreground pixels have a condition number greater than 10. To elucidate the impact of poor conditioning on optimization, we construct a simplified example of an ill-conditioned two-dimensional convex optimization problem, detailed in Appendix A.3. Even with  $\kappa = 10$ , convergence slows down drastically for an ill-conditioned convex optimization problem. This indicates severe ill-conditioning of the registration problem, strongly motivating the need for first-order adaptive optimization.

## 4.3 Adaptive Optimization for Diffeomorphisms

We provide a brief overview of the mathematical frameworks employed to optimize parameters that reside on Riemannian manifolds like diffeomorphisms, followed by a novel algorithm that exploits the group action to define a gradient descent algorithm that eliminates computationally expensive steps. This novel formulation of the ‘gradient descent’ algorithm can then be formulated to incorporate adaptive algorithms such as Adam <sup>26</sup> to optimize diffeomorphisms.

### 4.3.1 Euclidean gradient descent using the Lie algebra in shooting methods

Each Lie group has a corresponding Lie algebra  $\mathfrak{g}$  which is the tangent space at identity. This creates a locally one-to-one correspondence between elements of the group  $g \in G$  and elements of its Lie algebra  $v \in \mathfrak{g}$  given by the exponential map  $\exp : \mathfrak{g} \rightarrow G$ ; effectively to reach  $g = \exp(v)\text{id}$  from identity  $\text{id} \in G$ , the exponential map dictates that the group element has to move along  $v$  for unit time along the manifold. Exponential maps for many groups can be computed analytically, e.g., Rodrigues transformation for rotations, Jordan-Chevalley decomposition <sup>64</sup>, or the Cayley Hamilton theorem <sup>65</sup> for matrices. For diffeomorphisms, the Lie algebra is the space of all smooth velocity fields  $v : \Omega \rightarrow \mathbb{R}^d$ . There exist iterative methods to approximate the exponential map called the scaling-and-squaring approach <sup>17,32</sup> which uses the identity

$$\varphi = \exp(v) = \lim_{N \rightarrow \infty} \left( \text{id} + \frac{v}{N} \right)^N$$

to define a recursion by choosing  $N$  to be a large power of 2, i.e.  $N = 2^M$  as

$$\begin{aligned}\varphi^{(1/2^M)} &= id + v/2^M \\ \varphi^{(1/2^k)} &= \varphi^{(1/2^{(k+1)})} \circ \varphi^{(1/2^{(k+1)})} \quad \forall k \in \{0, 1, \dots, M-1\};\end{aligned}$$

This can be thought of as a special case of (5) with  $n = 2^M$ ,  $\epsilon = \frac{1}{n}$  and  $u_1 = \dots = u_n = v$ .

By virtue of the exponential map, we can solve the registration problem of finding  $\varphi \in G$  by directly optimizing over the Lie algebra  $v$ . This is because the Lie algebra is a vector space and we can perform, for example, standard Euclidean gradient descent for registration<sup>66–68</sup>. Such methods are called stationary velocity field or shooting methods. At each iteration, one uses the exponential map to get the transformation  $\varphi$  from the velocity field  $v$ , computes the gradient of the registration objective with respect to  $\varphi$ , pulls back this gradient into the tangent space where  $v$  lies

$$\nabla_v L = \frac{\partial \varphi}{\partial v} \nabla_\varphi L$$

and finally makes an update to  $v$ . Traditional methods like DARTEL<sup>17</sup> implement this approach. This is also very commonly used by deep learning methods for registration<sup>32,69,70</sup> due to its simplicity. Geodesic shooting methods are more sophisticated implementations of this approach where  $\varphi$  is the solution of a time-dependent velocity that follows the geodesic equation; the geodesic is completely determined by the initial velocity  $v_0 \in \mathfrak{g}$ .

Adaptive optimization algorithms can be applied to the Lie algebra since it is a Euclidean vector space  $\mathfrak{g}$ . However, there are a number of challenges with this method. First, this method requires computing the exponential map and its derivative, both of which need to be iteratively evaluated at each step of gradient descent. This is evident in Fig. 2 where direct optimization with ANTs runs much faster than the Lie-algebra counterpart. Moreover, the exponential map is only *locally* diffeomorphic, meaning it is suitable for modelling deviations close to the identity but not for large deformations – this leads to less expressivity and poor performance. In Fig. 2, the greedy SyN method which employs direct optimization significantly outperforms the Lie algebra-based DARTEL. In Fig. 16 we observed that across a large variety of hyper-parameters evaluated via grid search, direct optimization consistently led to better target overlap compared to its Lie algebra counterpart on the LPBA40 dataset. Therefore, we do not consider this method in our work.

### 4.3.2 Riemannian gradient descent

Solving the registration problem directly on the space of diffeomorphisms avoids repeated computations to and fro via the exponential map. The downside however is that one now has to explicitly account for the curvature and tangent spaces of the manifold. The updates for Riemannian gradient descent<sup>71</sup> at the  $t^{\text{th}}$  iteration are

$$\begin{aligned}\varphi_{t+1} &= \exp_{\varphi_t}(-\eta \text{Proj}_{\varphi_t}(\nabla_\varphi L)) \\ \text{where } \nabla_\varphi L &= \mathbf{g}_{\varphi_t}^{-1} \frac{\partial L}{\partial \varphi},\end{aligned}\tag{6}$$

where one pulls back the Euclidean gradient  $\frac{\partial L}{\partial \varphi}$  onto the manifold using the inverse metric tensor  $\mathbf{g}$  (which makes the gradient invariant to the parameterization of the manifold of diffeomorphisms)

before projecting it to the tangent space using  $\text{Proj}_{\varphi_t}$ . Since the tangent space is a local first-order approximation of the manifold’s surface, we can move along this descent direction by a step-size  $\eta$  and compute the updated diffeomorphism  $\varphi_{t+1}$ , represented as the exponential map from  $\varphi_t$  computed in the direction of  $-\text{Proj}_{\varphi_t}(\nabla_{\varphi} L)$ .

However, there are a few challenges in optimizing diffeomorphisms using Riemannian gradient descent. First, adaptive optimization algorithms such as RMSProp<sup>25</sup>, Adagrad<sup>72</sup> and Adam<sup>26</sup> have become popular because they can handle poorly conditioned optimization problems in deep learning. Variants for optimization on low-dimensional Riemannian manifold exist<sup>73–76</sup>. In contrast to these manifolds, diffeomorphisms are a high-dimensional variable-sized group (e.g., the parameterization of the warp field scales with that of the image size). Therefore, operations like computing the Riemannian metric tensor, and parallel transport of the optimization state variables (momentum and curvature) are very computationally expensive. For diffeomorphisms, computing the parallel transport requires solving a system of partial differential equations, which is computationally expensive. For these reasons, we do not consider direct Riemannian optimization for diffeomorphisms in our work.

#### 4.4 Exploiting the group structure of diffeomorphisms

Diffeomorphisms are imbued with additional structure compared to a Riemannian manifold – they are a Lie group as well. Not all Riemannian manifolds are Lie groups - notable examples of non-Lie group Riemannian manifolds include the sphere  $\mathbb{S}^n$ , fixed-rank matrices, and the Stiefel and Oblique manifolds<sup>71</sup>. The additional Lie group structure of  $G(\Omega, \mathbb{R}^d)$  allows us to exploit the group action to define a gradient descent algorithm that eliminates computationally expensive steps. In the following text, we provide a novel method to compute a descent direction in the group of diffeomorphisms that is computationally efficient and can be used with adaptive optimization algorithms.

**Minimizing the Eulerian differential.** Consider a function  $U : G \rightarrow \mathbb{R}$  that we aim to minimize. Let  $V$  be an admissible Hilbert space of vector fields on  $\Omega$  embedded in  $C_0^1(\Omega, \mathbb{R}^d)$ . We define an *Eulerian differential* in  $V$  if there exists a linear form  $\partial \bar{U} \in V^*$  such that for all  $v \in V$ :

$$(\partial \bar{U}(\varphi)|v)_E = \partial_t U(\varphi \circ \varphi_{0t}^v) \Big|_{t=0} \quad (7)$$

This definition of Eulerian differential is different from the one in<sup>61</sup> to perform all updates ( $v$ ) in the tangent space at identity and leverage Jacobian-free descent (see later). The goal is to choose a suitable  $v$  such that the directional change of the Eulerian differential along  $v$  is negative, making  $v$  a descent direction. A more familiar rate of change of  $U$  along a curve  $v$  is given by the *Gateaux derivative*:

$$\left( \frac{\partial U}{\partial \varphi} \Big| v \right)_G = \partial_t U(\varphi + tv) \Big|_{t=0} \quad (8)$$

The Eulerian differential is closely related to the Gateaux derivative of  $U$  at  $\varphi$  as:

$$(\partial \bar{U}(\varphi)|v)_E = \left( \frac{\partial U}{\partial \varphi} \Big| J(\varphi)v \right)_G$$

using chain rule. The right side is further expanded as:

$$(\partial \bar{U}(\varphi)|v)_E = \int_{\Omega} \left( \frac{\partial U}{\partial \varphi}(\varphi)(x) \right)^{\top} J(\varphi(x))v(x)dx$$

where  $J(\varphi)(x) = J(\varphi(x))$  with slight abuse of notation. We introduce the Gateaux derivative and relate it to the Eulerian derivative because we typically have access to the Gateaux derivative using automatic differentiation tools like PyTorch, but to perform optimization on the group of diffeomorphisms, we need to compute the Eulerian differential. Choosing

$$v_d(x) = -J(\varphi(x))^{\top} \frac{\partial U}{\partial \varphi}(\varphi)(x)$$

gives us:

$$(\partial \bar{U}(\varphi)|v_d)_E = - \int_{\Omega} \left\| J(\varphi)^{\top} \frac{\partial U}{\partial \varphi}(\varphi)(x) \right\|^2 dx < 0$$

This choice of  $v_d(x)$  is therefore a descent direction for the Eulerian differential of  $U$  at  $\varphi$ . To perform gradient descent on the Eulerian differential at  $\varphi$ , we need to compute the descent direction  $v_d$ , perform the exponential map with a small learning rate  $\eta_t$ , and perform the update:

$$\varphi_{t+1} = \varphi_t \circ \exp_{id}(\eta_t v_d)$$

For small enough  $\eta_t$ , the exponential map can be approximated with a retraction map (i.e.  $\exp_{id}(\eta_t v_d) \approx id + \eta_t v_d$ ), which is quick to compute.

We quickly contextualize the key differences between Gateaux gradient descent and our proposed Eulerian descent. First, the steepest descent direction in Gateaux gradient descent is  $-\frac{\partial U}{\partial \varphi}(\varphi)$ , whereas it is  $-J(\varphi)^{\top} \frac{\partial U}{\partial \varphi}(\varphi)$  in Eulerian descent. Second, the update rule in Gateaux gradient descent is  $\varphi_{t+1} = \varphi_t - \eta_t \frac{\partial U}{\partial \varphi}(\varphi)$ , whereas it is  $\varphi_{t+1} = \varphi_t \circ \exp_{id}(\eta_t v_d)$  in Eulerian descent. These two differences capture the essence of performing optimization on the group of diffeomorphisms in contrast to optimizing on the (Euclidean) ambient space directly.

**Adaptive optimization on diffeomorphisms.** Note that for small enough  $t$ , the descent direction  $v_d(x)$  can also be interpreted as a vector in the tangent space at identity, with  $\varphi_{0t}^v = \exp_{id}(tv)$  since  $\varphi_{00}^v = id$ , and  $\partial_t \varphi_{0t}^v|_{t=0} = v$ . Descent directions over gradient descent iterations  $i$  denoted as  $v_d^{(i)}$  all lie on the same vector space, i.e. the tangent space at identity. Therefore, first order algorithms like Adam can be applied on the sequence of descent directions  $v_d^{(i)}$  which now lie in the same vector space, without requiring computing the metric tensor, parallel transport or change of coordinates (charts) throughout the optimization process. This framework leveraging the group structure forms the core of our adaptive optimization algorithm for diffeomorphisms. Our framework is therefore a significant advantage over Riemannian optimization methods which require parallel transport of the momentum and curvature vectors at each iteration.

#### 4.4.1 Jacobian-Free Eulerian Descent

We provided an obvious choice of descent direction  $v_d(x)$  for the Eulerian differential of  $U$  at  $\varphi$ . The Gateaux derivative  $\frac{\partial U}{\partial \varphi}$  is readily obtained using automatic differentiation tools like PyTorch. However, the descent direction requires us to multiply this derivative with the Jacobian of the diffeomorphism  $J(\varphi)$ , which may be computationally expensive. However, in most diffeomorphic image registration applications, the role of the diffeomorphism is warp the image by performing local translations, scaling and shearing without introducing large local rotations. Mathematically, we consider the polar form of the Jacobian  $J(\varphi)(x) = U(x)P(x)$  where  $U(x)$  is a unitary matrix, and  $P(x)$  is a positive definite matrix. We assume that for most applications,  $U(x) \approx I_{d \times d}$ , making  $J(\varphi)(x)$  positive definite. With this assumption, we can choose the modified descent direction

$$v'_d(x) = -\frac{\partial U}{\partial \varphi}(\varphi)(x)$$

and the Eulerian differential at  $\varphi$  is

$$(\partial \bar{U} | v'_d)_E = - \int_{\Omega} \left( \frac{\partial U}{\partial \varphi}(\varphi)(x) \right)^{\top} J(\varphi(x)) \frac{\partial U}{\partial \varphi}(\varphi)(x) dx < 0$$

since  $v'_d(x)^{\top} J(\varphi(x)) v'_d(x) \geq 0$  for all  $x \in \Omega$ , owing to the (assumed) positive definiteness of  $J(\varphi)(x)$ . For all experiments, Jacobian-free descent directions  $v'_d(x)$  are used, and they provide faster runtime and with same accuracy. Adaptive first-order optimization can now be performed on this modified sequence on descent directions  $v_d^{(i)}(x)$ , saving significant computational and memory overhead by avoiding computation of  $J(\varphi)$ .

Note that this algorithm using the Eulerian differential is only possible due to the group structure of diffeomorphisms. For an arbitrary Riemannian manifold  $\mathcal{M}$  and points  $\varphi, \varphi_{0t}^v \in \mathcal{M}$ , the operation  $\varphi \circ \varphi_{0t}^v$  does not make sense. The additional group structure of  $G(\Omega, \mathbb{R}^d)$  allows us to propose a novel Eulerian descent algorithm without performing Lie algebra optimization, or Riemannian gradient descent, both of which are computationally expensive for diffeomorphisms.

#### 4.5 Interpolation strategies for multi-scale registration

Classical approaches to deformable image registration is performed in a multi-scale manner. Specifically, an image pyramid is constructed from the fixed and moving images by downsampling them at different scales, usually in increasing powers of two. Optimization is performed at the coarsest scale first, and the resulting transformation at each level is used to initialize the optimization at the next finer scale. Specifically, for the fixed image  $I$  and the moving image  $I'$  and  $K$  levels, let the downsampled versions be  $\{I_k\}_{k=1}^K$  and  $\{I'_k\}_{k=1}^K$ , where  $k$  is the scale index from coarsest to finest. At the  $k$ -th scale, the transformation  $\varphi_k$  is optimized as

$$\varphi_k^* = \operatorname{argmin}_{\varphi_k \in G} L(I_k, I'_k \circ \varphi_k)$$

where  $\varphi_k$  is initialized as

$$\varphi_k = \begin{cases} id & \text{if } k = 1 \\ \text{Upsample}(\varphi_{k-1}) & \text{otherwise} \end{cases}$$

Unlike existing gradient descent based approaches, our Riemannian adaptive optimizer also contains state variables  $m_k$  corresponding to the momentum and  $\nu_k$  corresponding to the EMA of squared gradient, at the same scale as  $\varphi_k$ , which require upsampling as well.

Unlike upsampling images, upsampling warp fields and their corresponding optimizer state variables requires careful consideration of the interpolation strategy. Bicubic interpolation is a commonly used strategy for upsampling images to preserve smoothness and avoid aliasing. However, bicubic interpolation of the warp field can lead to overshooting, leading to introducing singularities in the upsampled displacement field when there existed none in the original displacement field. In contrast, bilinear or trilinear interpolation does not lead to overshooting, and therefore diffeomorphism of the upsampled displacement is guaranteed, if the original displacement is diffeomorphic. We demonstrate this using a simple 2D warp field in [Fig. 13\(b\)](#). On the left, we consider a warp field created by nonlinear shear forces. This warp field does not contain any tears or folds - and is diffeomorphic. We upsample this warp field using bicubic interpolation (top) and bilinear interpolation (bottom). We also plot a heatmap of the negative of the determinant of the Jacobian of the upsampled warp, with a white contour representing the zero level set. Qualitatively, bicubic interpolation introduces noticeable folds in the warping field, leading to non-diffeomorphisms in the upsampled warp field. The heatmap shows a significant portion of the upsampled warp field has a negative determinant, indicating non-invertibility. On the other hand, bilinear interpolation looks blocky but preserves diffeomorphism everywhere, as also quantitatively verified by the absence of a zero level set in the heatmap.

The complete algorithm is described in [Algorithm 1](#).

---

**Algorithm 1** FireANTs

---

```
1: Input: Fixed image  $I_f$ , Moving image  $I_m$ 
2: Scales  $[s_1, s_2, \dots, s_n]$ , Iterations  $[T_1, T_2, \dots, T_n]$ ,  $n$  scales
3: optstate optimizer state (for Adam, RMSProp, etc.)
4: use_jac boolean specifying whether to use Jacobian in descent direction
5:
6: Initialize  $\varphi \leftarrow \text{id}_{s_1}$ . ▷ Initialize warp to identity at first scale
7: Initialize  $l \leftarrow 1$ . ▷ Initialize current scale
8: while  $l \leq n$  do
9:   Initialize  $i \leftarrow 0$ 
10:  Initialize  $I_f^l, I_m^l \leftarrow \text{downsample}(I_f, s_l), \text{downsample}(I_m, s_l)$ 
11:  while  $i < T_l$  do
12:     $U_i \leftarrow C(I_f^l, I_m^l \circ \varphi^i) + R(\varphi)$ 
13:    Compute  $v'_d(x) \leftarrow \frac{\partial U_i}{\partial \varphi}(\varphi^{(i)})(x)$  ▷ Jacobian-free Eulerian descent direction
14:    if use_jac then
15:      Compute  $v'_d(x) \leftarrow J^\top(\varphi^{(i)}(x))v'_d(x)$  ▷ Eulerian descent direction
16:    end if
17:    Update  $(v'_d(x), \text{optstate}) \leftarrow \text{optstate}(v'_d(x))$  ▷ Apply and update optimizer state
18:    Update  $\varphi^{(i+1)} \leftarrow \varphi^{(i)} \circ \exp_{id}(\epsilon_i v'_d) \approx \varphi^{(i)} \circ (id + \epsilon_i v'_d)$ 
19:     $i \leftarrow i + 1$ 
20:  end while
21:  if  $l < n$  then
22:     $\varphi \leftarrow \text{Upsample}(\varphi, s_{l+1})$  ▷ Upsample warp to next scale using bilinear/trilinear interpolation
23:  end if
24:   $l \leftarrow l + 1$ 
25: end while
```

---

**Figure 7: Algorithm for FireANTs** Algorithm 1 outlines the key steps in FireANTs - computing the Jacobian-free Eulerian descent direction which is simply the Gateaux derivative. If the boolean **use\_jac** is specified, then use the steepest Eulerian descent direction instead. This descent direction is then modified using any adaptive optimization algorithm denoted as **optstate**. The warp field is then updated using the exponential map or retraction map for small  $\epsilon_i$ . After optimization at a given scale, the warp field is upsampled using bilinear or trilinear interpolation to the next scale until optimization is complete for all steps.

## References

- [1] X. Wang, *Learning and Reasoning with Visual Correspondence in Time*. PhD thesis, Carnegie Mellon University, Pittsburgh, PA, September 2019.
- [2] M. S. Hamid, N. Abd Manap, R. A. Hamzah, and A. F. Kadmin, “Stereo matching algorithm based on deep learning: A survey,” *Journal of King Saud University-Computer and Information Sciences*, vol. 34, no. 5, pp. 1663–1673, 2022.

- [3] J. L. Carrivick, M. W. Smith, and D. J. Quincey, *Structure from Motion in the Geosciences*. John Wiley & Sons, 2016.
- [4] M. W. Smith, J. L. Carrivick, and D. J. Quincey, “Structure from motion photogrammetry in physical geography,” *Progress in physical geography*, vol. 40, no. 2, pp. 247–275, 2016.
- [5] R. Brunelli, *Template matching techniques in computer vision: theory and practice*. John Wiley & Sons, 2009.
- [6] H. Zhou and H. Hu, “Human motion tracking for rehabilitation—a survey,” *Biomedical signal processing and control*, vol. 3, no. 1, pp. 1–18, 2008.
- [7] F. Leon and M. Gavrilescu, “A review of tracking and trajectory prediction methods for autonomous driving,” *Mathematics*, vol. 9, no. 6, p. 660, 2021.
- [8] O. Van Kaick, H. Zhang, G. Hamarneh, and D. Cohen-Or, “A survey on shape correspondence,” in *Computer graphics forum*, vol. 30, pp. 1681–1707, Wiley Online Library, 2011.
- [9] J. Lee, D. Kim, J. Ponce, and B. Ham, “Sfnet: Learning object-aware semantic correspondence,” in *Proceedings of the IEEE/CVF Conference on Computer Vision and Pattern Recognition*, pp. 2278–2287, 2019.
- [10] F. Pomerleau, F. Colas, R. Siegwart, *et al.*, “A review of point cloud registration algorithms for mobile robotics,” *Foundations and Trends in Robotics*, vol. 4, no. 1, pp. 1–104, 2015.
- [11] D. Fortun, P. Bouthemy, and C. Kervrann, “Optical flow modeling and computation: A survey,” *Computer Vision and Image Understanding*, vol. 134, pp. 1–21, 2015.
- [12] A. Sotiras, C. Davatzikos, and N. Paragios, “Deformable medical image registration: A survey,” *IEEE transactions on medical imaging*, vol. 32, no. 7, pp. 1153–1190, 2013.
- [13] B. B. Avants, N. Tustison, G. Song, *et al.*, “Advanced normalization tools (ants),” *Insight j*, vol. 2, no. 365, pp. 1–35, 2009.
- [14] B. B. Avants, C. L. Epstein, M. Grossman, and J. C. Gee, “Symmetric diffeomorphic image registration with cross-correlation: evaluating automated labeling of elderly and neurodegenerative brain,” *Medical image analysis*, vol. 12, no. 1, pp. 26–41, 2008.
- [15] B. Avants and J. C. Gee, “Geodesic estimation for large deformation anatomical shape averaging and interpolation,” *Neuroimage*, vol. 23, pp. S139–S150, 2004.
- [16] M. F. Beg, M. I. Miller, A. Trouvé, and L. Younes, “Computing large deformation metric mappings via geodesic flows of diffeomorphisms,” *International journal of computer vision*, vol. 61, pp. 139–157, 2005.
- [17] J. Ashburner, “A fast diffeomorphic image registration algorithm,” *Neuroimage*, vol. 38, no. 1, pp. 95–113, 2007.
- [18] T. Vercauteren, X. Pennec, A. Perchant, N. Ayache, *et al.*, “Diffeomorphic demons using itk’s finite difference solver hierarchy,” *The Insight Journal*, vol. 1, 2007.

- [19] S. Bai, Z. Geng, Y. Savani, and J. Z. Kolter, “Deep equilibrium optical flow estimation,” in *Proceedings of the IEEE/CVF conference on computer vision and pattern recognition*, pp. 620–630, 2022.
- [20] G. Zhu, B. Jiang, L. Tong, Y. Xie, G. Zaharchuk, and M. Wintermark, “Applications of deep learning to neuro-imaging techniques,” *Frontiers in neurology*, vol. 10, p. 869, 2019.
- [21] W. Bai, H. Suzuki, J. Huang, C. Francis, S. Wang, G. Tarroni, F. Guitton, N. Aung, K. Fung, S. E. Petersen, *et al.*, “A population-based phenome-wide association study of cardiac and aortic structure and function,” *Nature medicine*, vol. 26, no. 10, pp. 1654–1662, 2020.
- [22] K. Murphy, B. Van Ginneken, J. M. Reinhardt, S. Kabus, K. Ding, X. Deng, K. Cao, K. Du, G. E. Christensen, V. Garcia, *et al.*, “Evaluation of registration methods on thoracic ct: the empire10 challenge,” *IEEE transactions on medical imaging*, vol. 30, no. 11, pp. 1901–1920, 2011.
- [23] I. Yoo, D. G. Hildebrand, W. F. Tobin, W.-C. A. Lee, and W.-K. Jeong, “ssemnet: Serial-section electron microscopy image registration using a spatial transformer network with learned features,” in *Deep Learning in Medical Image Analysis and Multimodal Learning for Clinical Decision Support: Third International Workshop, DLMIA 2017, and 7th International Workshop, ML-CDS 2017, Held in Conjunction with MICCAI 2017, Québec City, QC, Canada, September 14, Proceedings 3*, pp. 249–257, Springer, 2017.
- [24] A. Hand, T. Sun, D. Barber, D. Hose, and S. MacNeil, “Automated tracking of migrating cells in phase-contrast video microscopy sequences using image registration,” *Journal of microscopy*, vol. 234, no. 1, pp. 62–79, 2009.
- [25] T. Tieleman, G. Hinton, *et al.*, “Lecture 6.5-rmsprop: Divide the gradient by a running average of its recent magnitude,” *COURSERA: Neural networks for machine learning*, vol. 4, no. 2, pp. 26–31, 2012.
- [26] D. P. Kingma and J. Ba, “Adam: A method for stochastic optimization,” *arXiv preprint arXiv:1412.6980*, 2014.
- [27] Q. Wang, S.-L. Ding, Y. Li, J. Royall, D. Feng, P. Lesnar, N. Graddis, M. Naeemi, B. Facer, A. Ho, *et al.*, “The allen mouse brain common coordinate framework: a 3d reference atlas,” *Cell*, vol. 181, no. 4, pp. 936–953, 2020.
- [28] C. Xia, J. Fan, G. Emanuel, J. Hao, and X. Zhuang, “Spatial transcriptome profiling by merfish reveals subcellular rna compartmentalization and cell cycle-dependent gene expression,” *Proceedings of the National Academy of Sciences*, vol. 116, no. 39, pp. 19490–19499, 2019.
- [29] A. Klein, J. Andersson, B. A. Ardekani, J. Ashburner, B. Avants, M.-C. Chiang, G. E. Christensen, D. L. Collins, J. Gee, P. Hellier, *et al.*, “Evaluation of 14 nonlinear deformation algorithms applied to human brain mri registration,” *Neuroimage*, vol. 46, no. 3, pp. 786–802, 2009.
- [30] D. S. Marcus, T. H. Wang, J. Parker, J. G. Csernansky, J. C. Morris, and R. L. Buckner, “Open access series of imaging studies (oasis): cross-sectional mri data in young, middle aged, nondemented, and demented older adults,” *Journal of cognitive neuroscience*, vol. 19, no. 9, pp. 1498–1507, 2007.

- [31] A. Hering, L. Hansen, T. C. Mok, A. C. Chung, H. Siebert, S. Häger, A. Lange, S. Kuckertz, S. Heldmann, W. Shao, *et al.*, “Learn2reg: comprehensive multi-task medical image registration challenge, dataset and evaluation in the era of deep learning,” *IEEE Transactions on Medical Imaging*, vol. 42, no. 3, pp. 697–712, 2022.
- [32] G. Balakrishnan, A. Zhao, M. R. Sabuncu, J. Guttag, and A. V. Dalca, “Voxelmorph: a learning framework for deformable medical image registration,” *IEEE transactions on medical imaging*, vol. 38, no. 8, pp. 1788–1800, 2019.
- [33] M. Hoffmann, B. Billot, D. N. Greve, J. E. Iglesias, B. Fischl, and A. V. Dalca, “Synthmorph: learning contrast-invariant registration without acquired images,” *IEEE transactions on medical imaging*, vol. 41, no. 3, pp. 543–558, 2021.
- [34] N. L. S. T. R. Team, “Data from the national lung screening trial (nlst),” 2013.
- [35] L. Tian, H. Greer, R. Kwitt, F.-X. Vialard, R. San José Estépar, S. Bouix, R. Rushmore, and M. Niethammer, “unigradicon: A foundation model for medical image registration,” in *International Conference on Medical Image Computing and Computer-Assisted Intervention*, pp. 749–760, Springer, 2024.
- [36] Y. Liu, J. Chen, L. Zuo, A. Carass, and J. L. Prince, “Vector field attention for deformable image registration,” *Journal of Medical Imaging*, vol. 11, no. 6, pp. 064001–064001, 2024.
- [37] Y. Liu, L. Zuo, S. Han, Y. Xue, J. L. Prince, and A. Carass, “Coordinate translator for learning deformable medical image registration,” in *International workshop on multiscale multimodal medical imaging*, pp. 98–109, Springer, 2022.
- [38] V. Sivan, T. Vujovic, R. Ranabhat, A. Wong, S. McIlachlin, and M. Hardisty, “Recurrence with correlation network for medical image registration,” *arXiv preprint arXiv:2302.02283*, 2023.
- [39] “Rnr-exm grand challenge.”
- [40] T. Zheng, Z. Yang, A. Li, X. Lv, Z. Zhou, X. Wang, X. Qi, S. Li, Q. Luo, H. Gong, *et al.*, “Visualization of brain circuits using two-photon fluorescence micro-optical sectioning tomography,” *Optics express*, vol. 21, no. 8, pp. 9839–9850, 2013.
- [41] H. Gong, D. Xu, J. Yuan, X. Li, C. Guo, J. Peng, Y. Li, L. A. Schwarz, A. Li, B. Hu, *et al.*, “High-throughput dual-colour precision imaging for brain-wide connectome with cytoarchitectonic landmarks at the cellular level,” *Nature communications*, vol. 7, no. 1, p. 12142, 2016.
- [42] F. Chen, P. W. Tillberg, and E. S. Boyden, “Expansion microscopy,” *Science*, vol. 347, no. 6221, pp. 543–548, 2015.
- [43] G. M. Fleishman, “Bigstream.” <https://github.com/GFleishman/bigstream>, 2023. GitHub repository.
- [44] X. Jia, J. Bartlett, T. Zhang, W. Lu, Z. Qiu, and J. Duan, “U-net vs transformer: Is u-net outdated in medical image registration?,” *arXiv preprint arXiv:2208.04939*, vol. 1, 2022.

- [45] N. J. Tustison, M. Chen, F. N. Kronman, J. T. Duda, C. Gamlin, M. G. Tustison, M. Kunst, R. Dalley, S. Sorenson, Q. Wang, *et al.*, “The antsx ecosystem for mapping the mouse brain,” *bioRxiv*, pp. 2024–05, 2024.
- [46] GitHub, “Fireants github issues.” <https://github.com/rohittrango/FireANTs/issues/15>, 2024. GitHub repository issues.
- [47] GitHub, “Fireants github issues.” <https://github.com/rohittrango/FireANTs/pull/10>, 2024. GitHub repository issues.
- [48] O. Puonti, J. Nolan, R. Dicamillo, Y. Balbastre, A. Casamitjana, Matteo Mancini, E. Robinson, L. Peter, R. Annunziata, J. Althonayan, Shauna Crampsie, E. Blackburn, B. Billot, A. Atzeni, P. Schmidt, J. Hughes, J. Augustinack, B. Edlow, L. Zöllei, D. Thomas, D. Kliemann, Martina Bocchetta, C. Strand, J. Holton, Z. Jaunmuktane, and J. E. Iglesias, “An open-source tool for fast segmentation of any brain mr scan with the nextbrain histological atlas,” in *31th Annual Meeting of the Organization for Human Brain Mapping (OHBM 2025)*, 2025.
- [49] J. C. Gee and R. K. Bajcsy, “Elastic matching: Continuum mechanical and probabilistic analysis,” *Brain warping*, vol. 2, pp. 183–197, 1998.
- [50] S. C. Joshi and M. I. Miller, “Landmark matching via large deformation diffeomorphisms,” *IEEE transactions on image processing*, vol. 9, no. 8, pp. 1357–1370, 2000.
- [51] U. Grenander and M. I. Miller, “Computational anatomy: An emerging discipline,” *Quarterly of applied mathematics*, vol. 56, no. 4, pp. 617–694, 1998.
- [52] A. W. Toga and P. M. Thompson, “The role of image registration in brain mapping,” *Image and vision computing*, vol. 19, no. 1-2, pp. 3–24, 2001.
- [53] A. Gholipour, N. Kehtarnavaz, R. Briggs, M. Devous, and K. Gopinath, “Brain functional localization: a survey of image registration techniques,” *IEEE transactions on medical imaging*, vol. 26, no. 4, pp. 427–451, 2007.
- [54] F. A. Kronman, J. K. Liwang, R. Betty, D. J. Vanselow, Y.-T. Wu, N. J. Tustison, A. Bhandiwad, S. B. Manjila, J. A. Minter, D. Shin, *et al.*, “Developmental mouse brain common coordinate framework,” *bioRxiv*, 2023.
- [55] T. Sentker, F. Madesta, and R. Werner, “Gdl-fire: Deep learning-based fast 4d ct image registration,” in *International Conference on Medical Image Computing and Computer-Assisted Intervention*, pp. 765–773, Springer, 2018.
- [56] J. C. Gee, M. Reivich, and R. Bajcsy, “Elastically deforming a three-dimensional atlas to match anatomical brain images,” 1993.
- [57] G. E. Christensen and H. J. Johnson, “Consistent image registration,” *IEEE transactions on medical imaging*, vol. 20, no. 7, pp. 568–582, 2001.
- [58] E. Haber and J. Modersitzki, “Numerical methods for volume preserving image registration,” *Inverse problems*, vol. 20, no. 5, p. 1621, 2004.

- [59] A. Banyaga, *The structure of classical diffeomorphism groups*, vol. 400. Springer Science & Business Media, 2013.
- [60] J. Leslie, “On a differential structure for the group of diffeomorphisms,” *Topology*, vol. 6, no. 2, pp. 263–271, 1967.
- [61] L. Younes, *Shapes and diffeomorphisms*, vol. 171. Springer, 2010.
- [62] A. Mang and L. Ruthotto, “A lagrangian gauss–newton–krylov solver for mass-and intensity-preserving diffeomorphic image registration,” *SIAM Journal on Scientific Computing*, vol. 39, no. 5, pp. B860–B885, 2017.
- [63] A. Mang and G. Biros, “A semi-lagrangian two-level preconditioned newton–krylov solver for constrained diffeomorphic image registration,” *SIAM Journal on Scientific Computing*, vol. 39, no. 6, pp. B1064–B1101, 2017.
- [64] C. Chevalley, “Théorie des groupes de lie,” (*No Title*), 1951.
- [65] B. Mertzios and M. Christodoulou, “On the generalized cayley-hamilton theorem,” *IEEE transactions on automatic control*, vol. 31, no. 2, pp. 156–157, 1986.
- [66] C. Moler and C. Van Loan, “Nineteen dubious ways to compute the exponential of a matrix, twenty-five years later,” *SIAM review*, vol. 45, no. 1, pp. 3–49, 2003.
- [67] B. C. Hall and B. C. Hall, *Lie groups, Lie algebras, and representations*. Springer, 2013.
- [68] B. C. Hall, “An elementary introduction to groups and representations,” *arXiv preprint math-ph/0005032*, 2000.
- [69] J. Krebs, H. Delingette, B. Mailhé, N. Ayache, and T. Mansi, “Learning a probabilistic model for diffeomorphic registration,” *IEEE transactions on medical imaging*, vol. 38, no. 9, pp. 2165–2176, 2019.
- [70] M. Niethammer, R. Kwitt, and F.-X. Vialard, “Metric learning for image registration,” in *Proceedings of the IEEE/CVF Conference on Computer Vision and Pattern Recognition*, pp. 8463–8472, 2019.
- [71] N. Boumal, B. Mishra, P.-A. Absil, and R. Sepulchre, “Manopt, a Matlab toolbox for optimization on manifolds,” *Journal of Machine Learning Research*, vol. 15, no. 42, pp. 1455–1459, 2014.
- [72] J. Duchi, E. Hazan, and Y. Singer, “Adaptive subgradient methods for online learning and stochastic optimization.,” *Journal of machine learning research*, vol. 12, no. 7, 2011.
- [73] S. Bonnabel, “Stochastic gradient descent on riemannian manifolds,” *IEEE Transactions on Automatic Control*, vol. 58, no. 9, pp. 2217–2229, 2013.
- [74] H. Zhang, S. J Reddi, and S. Sra, “Riemannian svrg: Fast stochastic optimization on riemannian manifolds,” *Advances in Neural Information Processing Systems*, vol. 29, 2016.
- [75] G. Bécigneul and O.-E. Ganea, “Riemannian adaptive optimization methods,” *arXiv preprint arXiv:1810.00760*, 2018.

- [76] M. Kochurov, R. Karimov, and S. Kozlukov, “Geoopt: Riemannian optimization in pytorch,” 2020.
- [77] A. C. Evans, D. L. Collins, S. Mills, E. D. Brown, R. L. Kelly, and T. M. Peters, “3d statistical neuroanatomical models from 305 mri volumes,” in *1993 IEEE conference record nuclear science symposium and medical imaging conference*, pp. 1813–1817, IEEE, 1993.

## A Supplementary Information

### A.1 Datasets used in Klein *et al.* challenge

Brain image data and their corresponding labels for 80 normal subjects were acquired from four different datasets. The *LPBA40* dataset contains 40 brain images and their labels to construct the LONI Probabilistic Brain Atlas (LPBA40). All volumes were skull-stripped, and aligned to the MNI305 atlas<sup>77</sup> using rigid-body transformation to correct for head tilt. For all these subjects, 56 structures were manually labelled and bias-corrected using the BrainSuite software. The *IBSR18* dataset contains brain images acquired at different laboratories through the Internet Brain Segmentation Repository. The T1-weighted images were rotated to be in Talairach alignment and bias-corrected. Manual labelling is performed resulting in 84 labeled regions. For the *CUMC12* dataset, 12 subjects were scanned at Columbia University Medical Center on a 1.5T GE scanner. Images were resliced, rotated, segmented and manually labeled, leading to 128 labeled regions. Finally, the *MGH10* dataset contains 10 subjects who were scanned at the MGH/MIT/HMS Athinoula A. Martinos Center using a 3T Siemens scanner. The data is bias-corrected, affine-registered to the MNI152 template, and segmented. Finally the images were manually labeled, leading to 74 labeled regions. All datasets have a volume of  $256 \times 256 \times \{128, 124\}$  voxels with varying amounts of anisotropic voxel spacing, ranging from  $0.84 \times 0.84 \times 1.5\text{mm}$  to  $1 \times 1 \times 1.33\text{mm}$ .

### A.2 Modular software implementation to enable effective experimentation

Registration is a key part of many data processing pipelines in the clinical literature. Our software implementation is designed to be extremely flexible, e.g., it implements a number of existing registration methods using our techniques, modular, e.g., the user can choose different group representations (rigid or affine transforms, diffeomorphisms), objective functions, optimization algorithms, loss functions, and regularizers. Users can also stack the same class of transformations, but with different cost functions. For example, they can fit an affine transform using label maps and Dice loss, and use the resultant affine matrix as initialization to fit another affine transform using the cross-correlation registration objective. This enables seamless tinkering and real-time investigation of the data. Deformations can also be composed in increasing order of complexity (rigid  $\rightarrow$  affine  $\rightarrow$  diffeomorphisms), thereby avoiding multiple resampling and subsequent resampling artifacts. We have developed a simple interface to implement custom cost functions, which may be required for different problem domains, with ease; these custom cost functions can be used for any of the registration algorithms out-of-the-box. Our implementation can handle images of different sizes, anisotropic spacing, without the need for resampling into a consistent physical spacing or voxel sizes. All algorithms also support multi-scale optimization (even with fractional scales) and convergence monitors for early-stopping.

Our software is implemented completely using default primitives in PyTorch. All code and example scripts is available at

<https://github.com/rohittrango/fireants>.

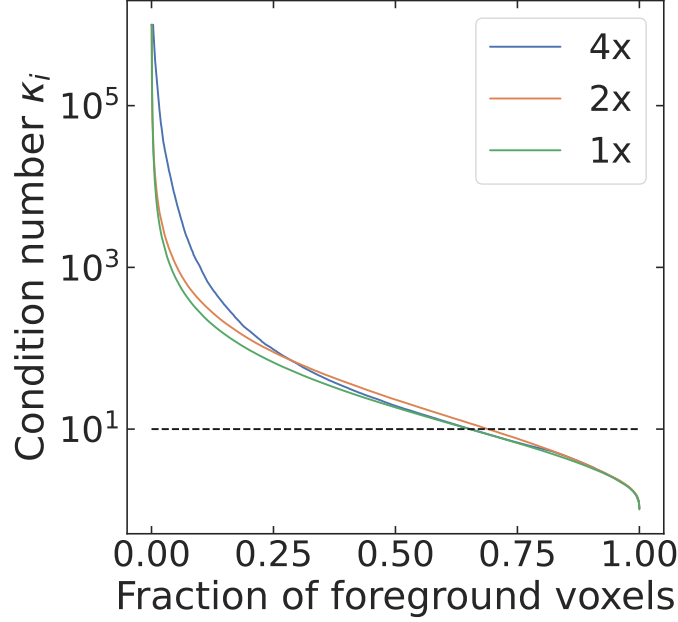


**Figure 8: Deformable image registration is ill-conditioned.** To quantitatively examine ill-conditioning in registration, we compute the distribution of per-pixel condition number for a MRI registration task, at different image downsampling factors (denoted as 1x, 2x, and 4x). A high condition number signifies exacerbated ill conditioning and requires higher-order optimization. A horizontal dashed line denoting  $\kappa = 10$  is drawn as a reference for substantial ill conditioning. Across all scales, a substantial fraction of foreground voxels are ill-conditioned ( $\kappa > 10$ ), necessitating adaptive first-order optimization for faster convergence and accurate registration.

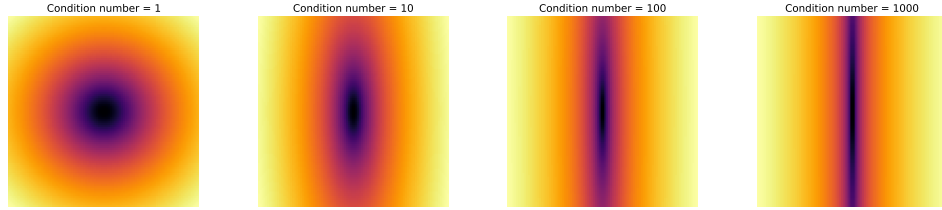
### A.3 On the Ill-conditioning of Image Registration

Image registration is a highly ill-conditioned, and non-convex problem necessitating advanced optimization methods for convergence. To provide more intuition on the effect of  $\kappa$  on convergence of the SGD algorithm, we consider a toy example of a 2D optimization problem. Specifically, we consider a loss function  $f_\kappa(x, y) = x^2 + \kappa y^2$  where  $\kappa > 1$  becomes the condition number of the problem. Qualitatively, the effect of the first term diminishes exponentially fast with  $\kappa$  (Fig. 9a). Quantitatively, we run both SGD and Adam optimization for a 1000 iterations starting from the point  $(x, y) = (5, 5)$ . Fig. 9c shows that SGD works extremely well for  $\kappa = 1$  which is the best-conditioned loss function, but quickly gets stuck for  $\kappa \geq 100$ . On the contrary, Adam is invariant to the condition number and converges to the minima for all values of  $\kappa$ . This is because for a diagonal Hessian (as in this case), the second-order adaptive terms are proportional to the diagonal elements of the Hessian. These condition numbers are vanishingly small compared to those in typical image registration tasks, which can exceed  $10^5$ , making them extremely ill-conditioned.

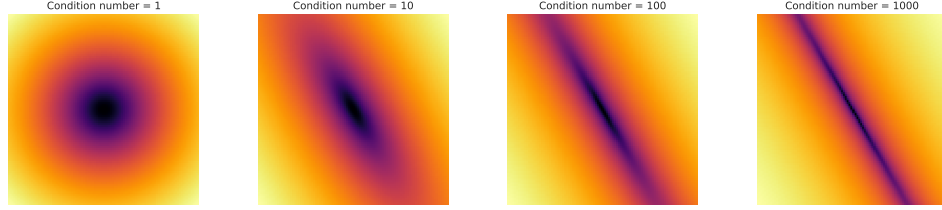
We also consider a more realistic, but tractable scenario of the convex loss function  $f_{\kappa, \theta}(x, y) = x_\theta^2 + \kappa y_\theta^2$ , where

$$\begin{bmatrix} x_\theta \\ y_\theta \end{bmatrix} = \begin{bmatrix} \cos(\theta) & \sin(\theta) \\ -\sin(\theta) & \cos(\theta) \end{bmatrix} \begin{bmatrix} x \\ y \end{bmatrix}$$

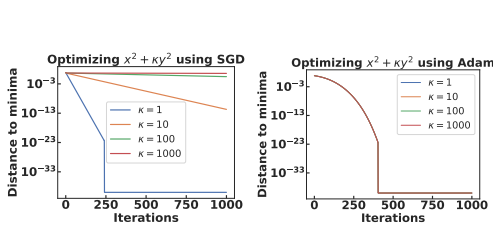
We choose  $\theta = \pi/3$  for this experiment. This is simply a rotated version of the previous family of loss functions, as shown in Fig. 9b. The trajectories obtained from optimization using SGD (Fig. 9d) are virtually identical to that in Fig. 9c since the new gradients are simply rotated versions of the previous gradients, and the distance from the minima is invariant to the rotation. However, the trajectories from Adam optimization are qualitatively very different, owing to the increasing difference between the true Hessian and its diagonal approximation. Even so, the final point is at a distance of less than  $10^{-3}$  units to the minima for  $\kappa = 1000$ , showing the effectiveness of adaptive optimization even for ill-conditioned, non-diagonal Hessians. This is a strong motivation to extend adaptive optimization for non-Euclidean diffeomorphic registration, which is very high-dimensional and ill-conditioned.



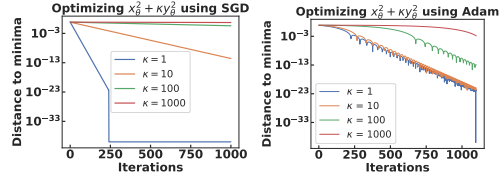
(a) Log-Loss landscape of the toy problem  $f_\kappa(x, y) = x^2 + \kappa y^2$  for  $\kappa = 1, 10, 100, 1000$ . The log-loss becomes increasingly sharp along the  $y$ -direction as  $\kappa$  increases.



(b) Log-Loss landscape of the toy problem  $f_\kappa(x, y) = x_\theta^2 + \kappa y_\theta^2$  for  $\kappa = 1, 10, 100, 1000$ , where  $(x_\theta, y_\theta)$  is the coordinate  $(x, y)$  rotated by an angle  $\theta$  about the origin.



(c) Optimization of Fig. 9a using SGD and Adam shows that SGD fails to recover the minima for  $\kappa \geq 100$  while Adam is *invariant* to the condition number for diagonal Hessian matrices. This is a strong motivation to use first order adaptive optimization for registration where the condition number can exceed  $10^5$ .

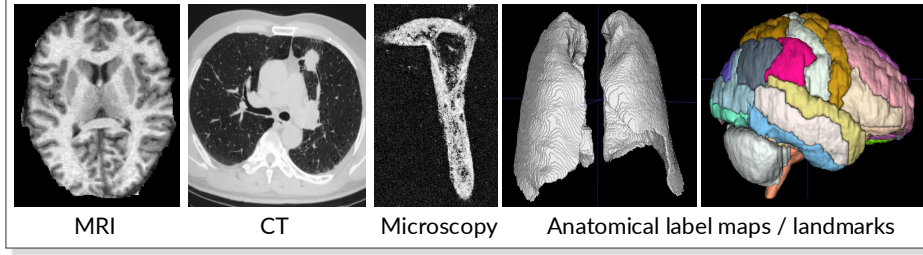


(d) Optimization of Fig. 9b using SGD shows identical optimization trajectories as Fig. 9c. Adam, however, is not invariant to the condition number because the difference between the true Hessian and its diagonal approximation increases with  $\kappa$ . Even so, the final point is at a distance of less than  $10^{-3}$  units to the minima, showing the mitigating effect of adaptive optimization even for non-diagonal Hessians.

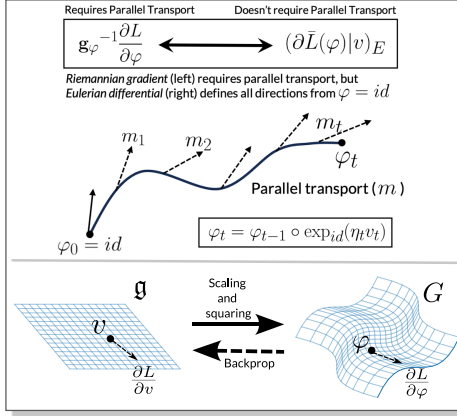
**Table 1: Quantitative performance on OASIS validation set.** FireANTs performs competitively with state-of-the-art registration methods on the OASIS dataset on both Dice Overlap and Hausdorff distance.

<b>Validation metrics on OASIS</b>		
<b>Method</b>	<b>Dice</b>	<b>HD95</b>
Affine (Baseline)	$0.572 \pm 0.051$	$3.831 \pm 0.718$
ANTs <sup>13</sup>	$0.786 \pm 0.033$	$2.209 \pm 0.534$
VoxelMorph <sup>32</sup>	$0.753 \pm 0.145$	-
LogDemons <sup>18</sup>	$0.804 \pm 0.022$	$2.068 \pm 0.448$
SynthMorph <sup>33</sup>	$0.785 \pm 0.023$	$2.311 \pm 0.452$
FireANTs	$0.791 \pm 0.028$	$2.793 \pm 0.602$

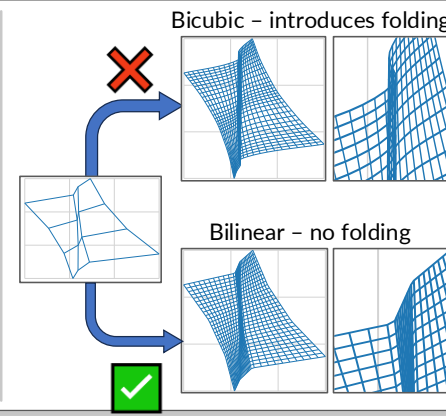
### (a) Supported data types and modalities



### (b) Adaptive optimization



### (c) Multiscale considerations



### (d) Ease of experimentation

<p><b>Speed</b></p> <ul style="list-style-type: none"> <li>➤ ~2000x speedup on MRI brain datasets</li> <li>➤ Up to 1200x speedup - lung CT</li> <li>➤ Makes hyperparameter tuning tractable</li> </ul>	<p><b>Accuracy</b></p> <ul style="list-style-type: none"> <li>➤ State-of-the-art performance on four community reference brain datasets</li> <li>➤ Best fissure alignment in lung data challenge</li> <li>➤ First place in RnR ExM mouse brain</li> </ul>	<p><b>Robustness</b></p> <ul style="list-style-type: none"> <li>➤ Across hyperparameters – low sensitivity of dice score</li> <li>➤ Across datasets – Performance does not collapse for specific data</li> </ul>	<p><b>Tunability</b></p> <ul style="list-style-type: none"> <li>➤ Representation</li> <li>➤ Loss function</li> <li>➤ Customizable</li> <li>➤ Optimizer</li> </ul> <p><b>Composability</b></p> $\varphi_1 \leftarrow r_1, l_1, o_1$ $\varphi_2 \leftarrow r_2, l_2, o_2$ <p>...</p> $\varphi = \varphi_N^* \circ \dots \circ \varphi_2^* \circ \varphi_1^*$
--	---	--	--

**Figure 10: Overview of FireANTs and its features:** (a) shows the modalities our method is tested on. We demonstrate results on in-vivo T1-weighted brain MRI, lung CT, and expansion microscopy volumes. FireANTs can optimize intensity images as well as binary masks (lung masks in CT) or entire anatomical label maps (brain MRI). (b) shows the technical contributions of FireANTs. We extend Adaptive Optimization to multi-scale Diffeomorphisms by first writing the Riemannian gradient update, and then avoiding parallel transport of the optimization state by leveraging the interchangeability of the Riemannian gradient at arbitrary transform  $\varphi_t$  with the Riemannian gradient at  $\varphi = Id$ . For the Lie-algebra representation, the Gateaux derivative  $\frac{\partial L}{\partial \varphi}$  is projected to  $\frac{\partial L}{\partial v}$  using analytical backprop. Since the Lie algebra is a vector space, we use standard adaptive optimizers (see §4.3.2 for more details). (c) takes a closer look at multi-scale interpolation for diffeomorphisms represented as a warp field. Bicubic interpolation can introduce folding of the warp field at a finer resolution due to overshooting, but bilinear interpolation does not. Therefore, we use this for interpolating the warp field and the optimizer state. (d) shows the extensive experimental setup. Our method is orders of magnitude faster, has state-of-the-art performance on 3 challenges, is robust across hyperparameters and datasets, and is modular and easy to extend.

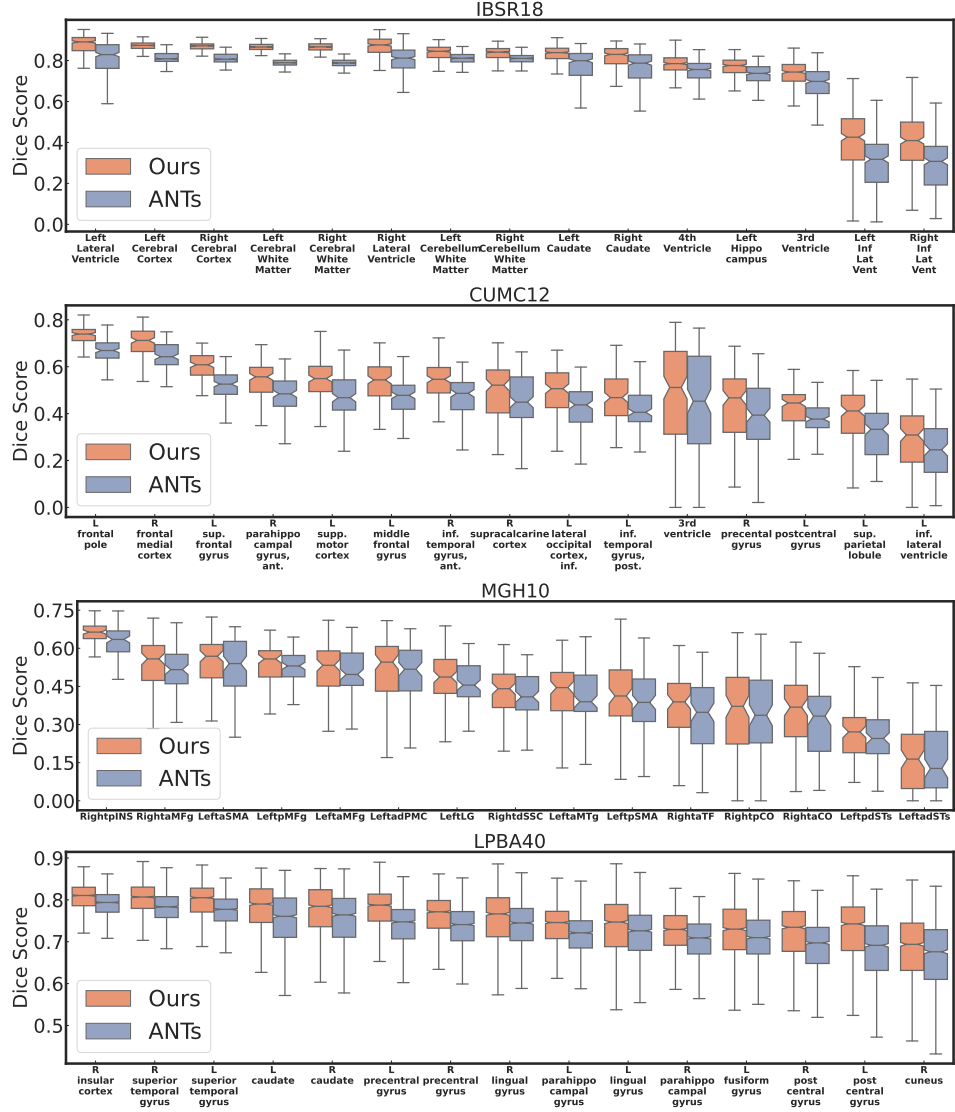


**Figure 11: Regionwise target overlap on the brain MRI datasets:** We further evaluate regionwise overlap scores by sampling 15 regions from each dataset, and comparing their distribution using our method and ANTs. Our method has a much higher median score, and better interquartile ranges across regions, demonstrating both accuracy and robustness.

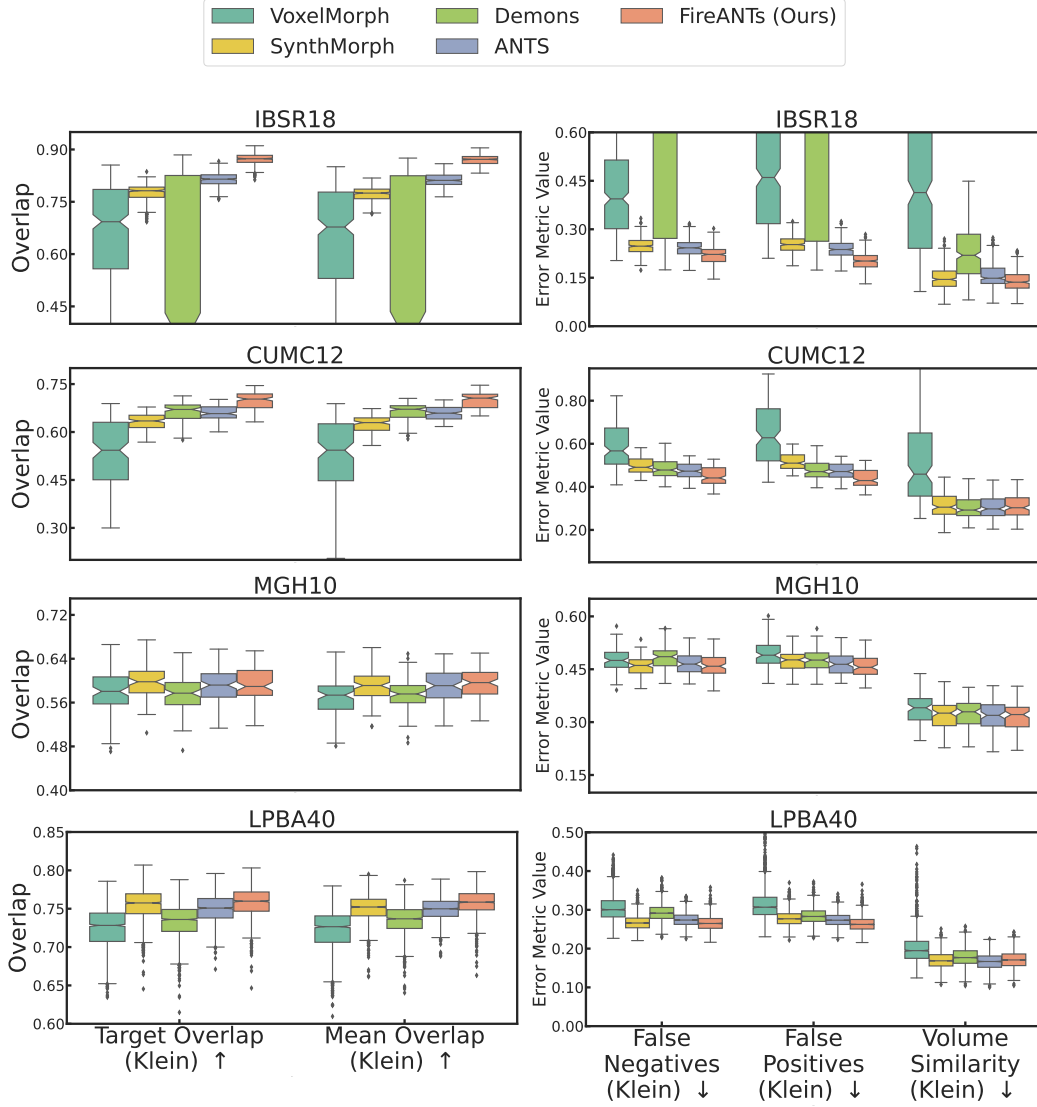


**Figure 12: Comparison of our method with ANTs on 4 MRI brain datasets:** Registration quality is validated by measuring volume overlap of label maps between the fixed and warped label maps. **(a):** For anatomical region  $r$ , warped (binary) label map  $S_r$  and fixed label map  $T_r$ , target and mean overlap are defined as  $|S_r \cap T_r|/|T_r|$  and  $2|S_r \cap T_r|/(|S_r| + |T_r|)$ . We define the aggregate target overlap over all anatomical regions as  $\sum_r (|S_r \cap T_r|/|T_r|)$  and Klein *et al.*<sup>29</sup> define it as  $(\sum_r |S_r \cap T_r|)/(\sum_r |T_r|)$ , likewise for other metrics. The latter aggregation is denoted with the suffix (Klein) in the figure. In all four datasets, the boxplots show a narrower interquartile range and substantially higher median than ANTs (higher is better), underscoring the stability and accuracy of our algorithm. **(b):** Other measures of anatomical label overlap used in<sup>29</sup> are false positives ( $|T_r \setminus S_r|/|T_r|$ ), false negatives ( $|S_r \setminus T_r|/|S_r|$ ), and volume similarity ( $2(|S_r| - |T_r|)/(|S_r| + |T_r|)$ ) (lower is better). We observe similar trends as in (a), with a narrower interquartile range and substantially lower median values. Results of per region overlap metrics are in the Fig. 11.

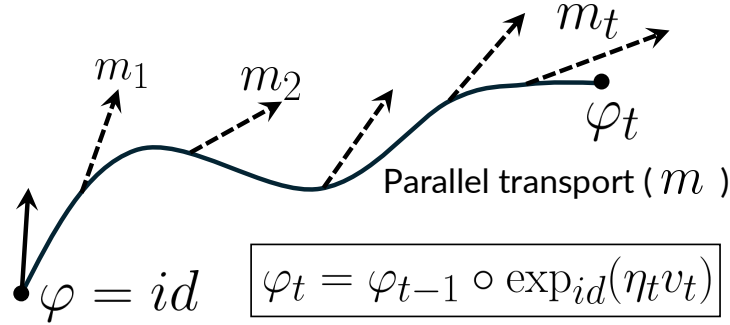
(a) Trick to avoid parallel transport in Riemannian Adaptive Optimization using Eulerian differentials

Requires Parallel Transport

Does not require Parallel Transport

$$\mathbf{g}_\varphi^{-1} \frac{\partial L}{\partial \varphi} \longleftrightarrow (\partial \bar{L}(\varphi)|v)_E$$

Riemannian gradient (left) requires parallel transport, but Eulerian differential (right) defines all directions from  $\varphi = id$



(b) Bicubic interpolation of diffeomorphic map does not preserve diffeomorphism

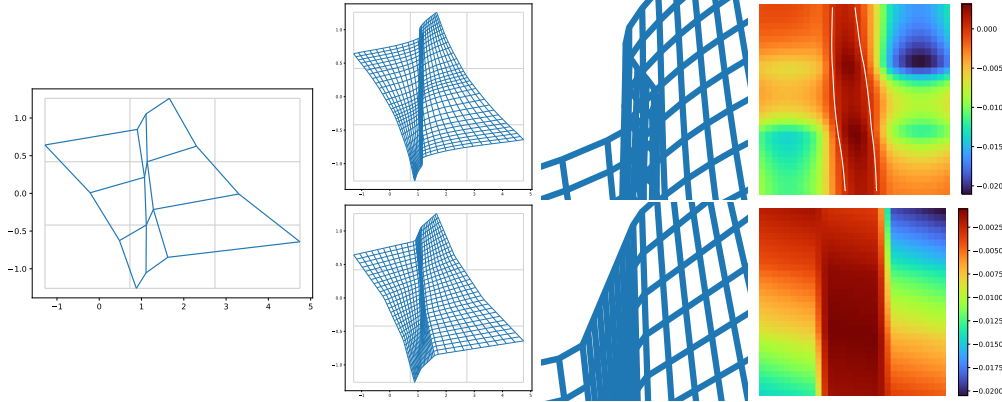


**Figure 13: Overview of tricks for multi-scale adaptive optimization for diffeomorphisms:** (a) We exploit the group structure of diffeomorphisms to define an Eulerian differential that avoids the need for parallel transport in adaptive optimization algorithms. (b) We show the effect of downsampling on the warp and determinant of the Jacobian for a single image pair. The first column shows the initial warp, and the second and third columns show the warp and determinant of the Jacobian for the cubic and bilinear interpolations, respectively.

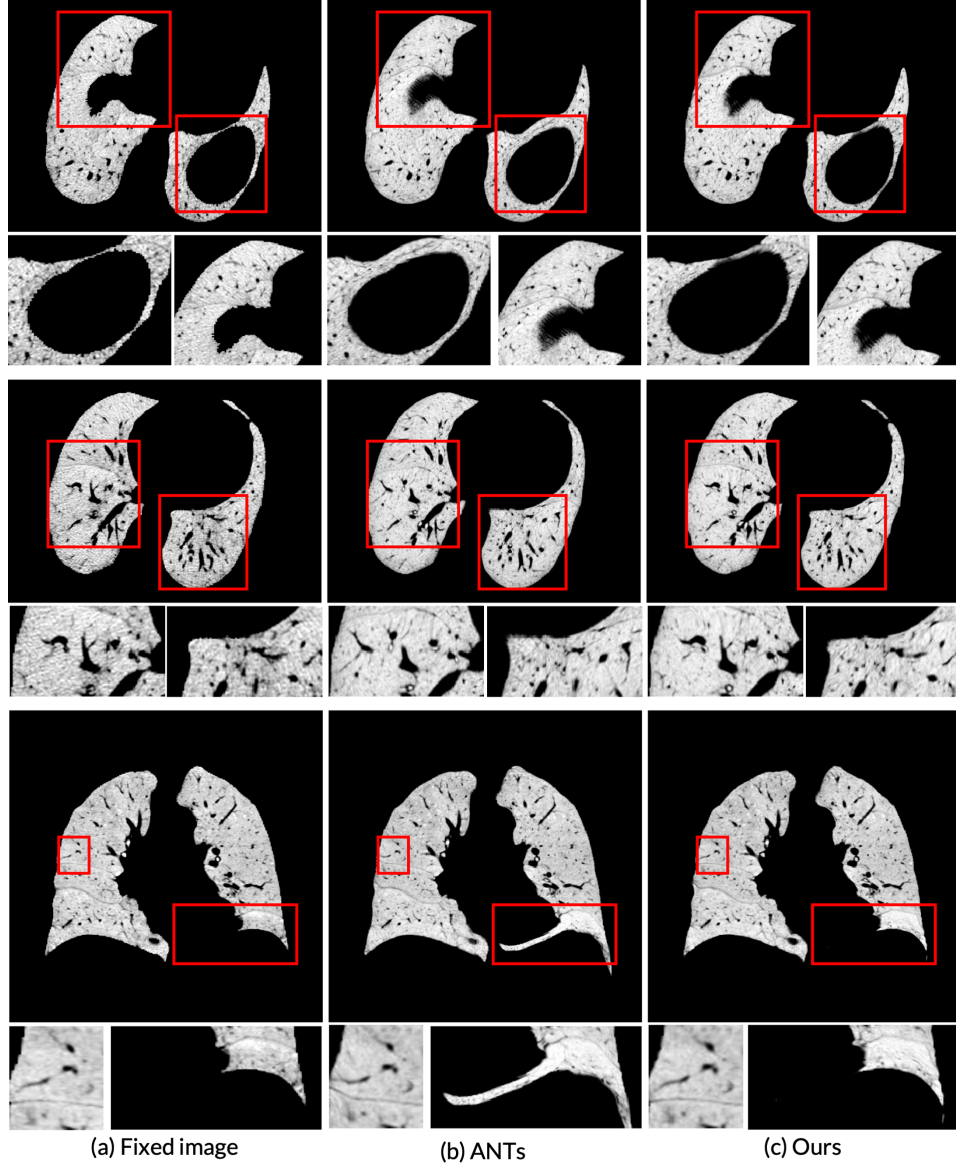


**Figure 14: Qualitative results on EMPIRE10 challenge:** (a) shows the fixed image, (b) shows the registration performed by ANTs, and (c) our method, all with zoomed in regions. ANTs performs a coarse registration with ease, but still leaves out critical alignment of lung boundary and airways by not utilizing adaptive optimization. Our method performs *perfectly* diffeomorphic registration by construction, and does not lead to any registration errors, both in the lung boundaries or internal features.

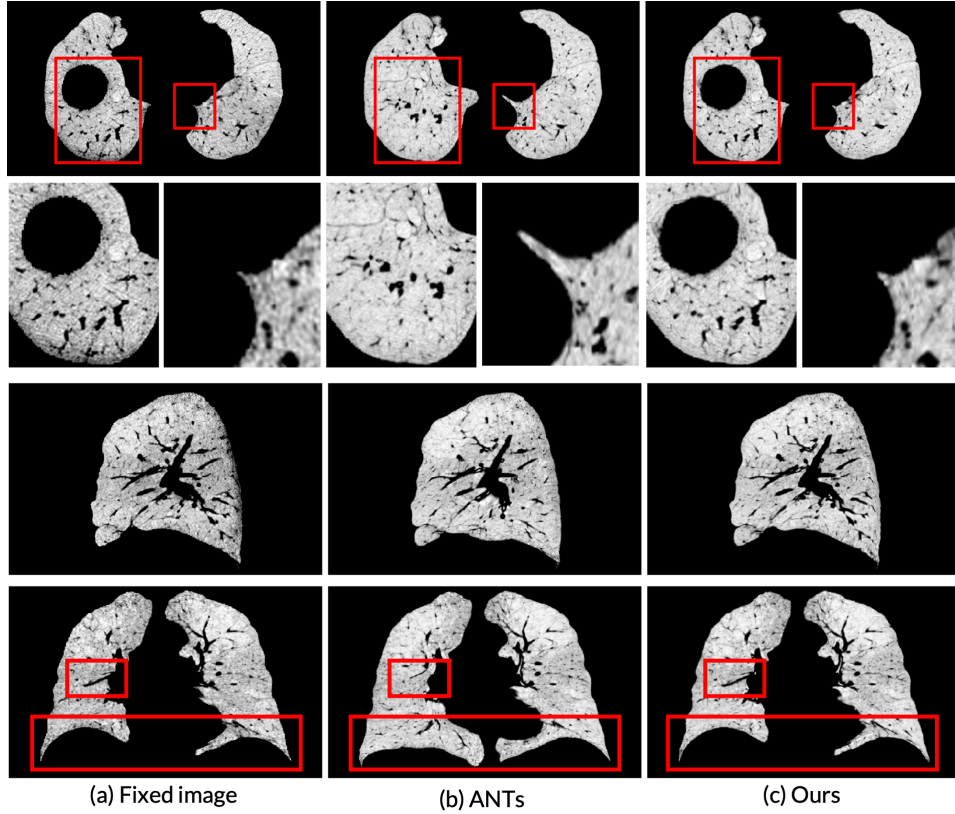


**Figure 15: More Qualitative results on EMPIRE10 challenge:** (a) shows the fixed image, (b) shows the registration performed by ANTs, and (c) our method, all with zoomed in regions. ANTs performs a coarse registration with ease, but still leaves out critical alignment of lung boundary and airways by not utilizing adaptive optimization. Our method performs *perfectly* diffeomorphic registration by construction, and does not lead to any registration errors, both in the lung boundaries or internal features.

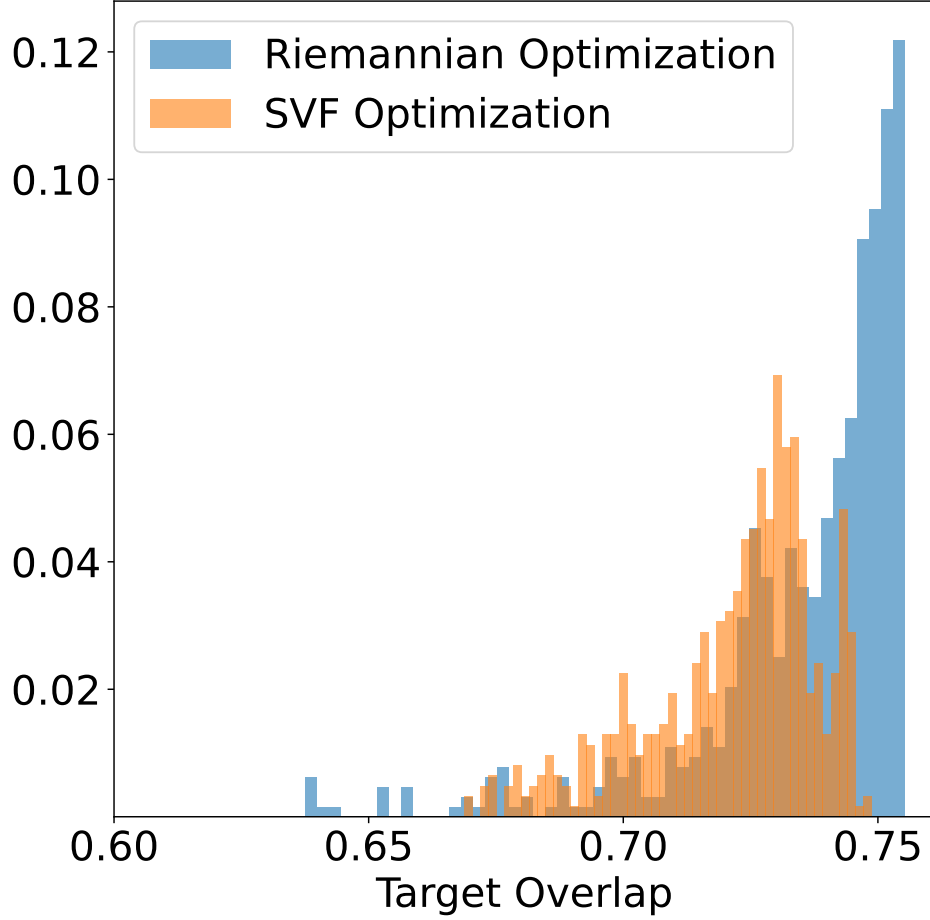


**Figure 16: Comparison of exponential versus direct optimization on LPBA40 dataset:** We run the hyperparameter grid search on the LPBA40 dataset using direct Riemannian gradient updates with Adam optimizer (denoted as *rgd*), and optimizing the velocity field by computing the exponential map to represent the diffeomorphism (denoted as *exp*) across all the configurations shown in Fig. 5(a). The average target overlap for each configuration is then stored, and a histogram of target overlap values of the dataset is constructed. Note that the *rgd* variant has a significantly more number of configurations near the optimal value, and the average performance and the overall distribution of our optimization is better for the *rgd* variant than *exp*. Similar trends can be observed for the EMPIRE10 lung challenge in Fig. 2, where the *exp* representation underperforms for the same cost function, data, etc. Therefore, we recommend direct RGD optimization for diffeomorphisms.